DESIGN OF YBCO-BASED MACHINES USING 2D METHOD OF MOMENTS

by

Kyle Waggoner

A Thesis

Submitted to the Faculty of Purdue University

In Partial Fulfillment of the Requirements for the degree of

Master of Science

School of Electrical and Computer Engineering

West Lafayette, Indiana

May 2021

THE PURDUE UNIVERSITY GRADUATE SCHOOL
STATEMENT OF COMMITTEE APPROVAL

Dr. Steven Pekarek, Chair

School of Electrical and Computer Engineering

Dr. Scott Sudhoff

School of Electrical and Computer Engineering

Dr. Michael Melloch

School of Electrical and Computer Engineering

Approved by:

Dr. Dimitrios Peroulis

Head of Electrical and Computer Engineering

ACKNOWLEDGMENTS

I would like to thank each of my committee members, Professors Pekarek, Sudhoff, and Melloch, for their support in this research and for contributing to my education at Purdue. I would like to express my sincere gratitude to Professor Pekarek for all of his support and guidance these past couple years, and also for prompting my interest in pursuing graduate school in the first place. I would also like to thank Professors Aliprantis and Wasynczuk for their contributions to my education at Purdue, both in my graduate and undergraduate studies.

TABLE OF CONTENTS

LIST OF TABLES

LIST OF FIGURES

ABSTRACT

In this research, the use of a Type-2 superconducting material (i.e. Yttrium Barium Copper Oxide) as a magnetic flux source within synchronous machines is considered. To do so, an analytical model is applied to predict the magnetic field and the currents that are induced within the material when it is magnetized to a mixed-state. These induced currents are then used to model the synchronous machine performance within a 2-dimensional Method of Moments (MoM) formulation. The MoM-based model is used in tandem with a thermal equivalent circuit to calculate the cooling required to keep the YBCO below its critical temperature. These are utilized within a genetic algorithm (GA) to evaluate the tradeoffs between mass and loss for several example electric drives ranging from 10 kW-20 MW. The expected mass and loss of the YBCO machines are compared to those of a standard permanent magnet synchronous machine (PMSM). Specifically, Pareto-optimal fronts are used to assess power levels where cryo-cooled YBCO materials may be warranted.

1. YBCO BACKGROUND

1.1 Introduction to Superconductors

Superconducting materials were discovered over 100 years ago. They received their name due to the fact that if the material is cooled below a critical temperature T_c, a state of zero electrical resistance is achieved. This property has motivated their use in a wide range of applications, from electrical conductors [1], [2], motors and generators [3]–[11], and magnetic levitation [12], [13]. However, one of the main obstacles of their application is that historically, the critical temperature required to achieve superconductivity was very low. As a result liquid helium, which has a boiling point of 4.2 K [14], had to be used in order to cool the materials below their critical temperature.

This motivated the discovery of high-temperature superconductors (HTS) [15]. A HTS material with a higher critical temperature was discovered by researchers in [16]. The material was created using a compound composed of yttrium, barium, copper, and oxygen. This Y-Ba-Cu-O compound, or YBCO, as it is commonly abbreviated, has a critical temperature of 93 K. Its molecular chemical composition is $YBa_2Cu_3O_{7-x}$, thus it is also sometimes referred to as Y123. The significance of this material is that it can be cooled using liquid nitrogen, which has a boiling point of 77 K. This property makes HTS like YBCO a popular choice in many modern applications.

1.2 Properties of YBCO

One of the main properties of superconductors is that due to the Meissner effect, the magnetic field $\mathbf{B}$ inside a material in a superconducting state is zero. This occurs because when an external field is applied to the material in a superconductive state, electric current is induced on its surface to produce an opposing field, resulting in all of the internal flux being cancelled [17]. Related to the Meissner effect, superconductors also have a critical field, H_c, and a corresponding critical current I_c (or critical current density J_c) . The critical field H_c is the maximum external field that can be applied to the material before it is no longer in a superconducting state [18]. A field higher than H_c would yield currents higher than can be produced within the superconductor. According to [18], since this surface current cannot be distinguished from a magnetic moment, superconductors are often represented as having a negative magnetization.

All superconductors exhibit the Meissner effect, however superconducting materials are typically categorized as Type I or Type II. Type I materials have a single critical field H_c that is temperature dependent. Increasing the field above H_c returns the material to a normal, non-superconducting state. However, Type II superconductors, of which YBCO belongs, have two critical fields H_{c1} and H_{c2}. Specifically, they exhibit the Meissner effect up until the critical field H_{c1}. If the external field increases above H_{c1}, the material transitions to a mixed or vortex state, where magnetic flux can begin to penetrate the superconductor. In [19], it is stated that if the field is increased above H_{c1} then there are areas of the superconductor with nonzero magnetic flux, and that these areas have induced currents circulating around the flux lines. As the external field is further increased, more flux penetrates the material and it transitions from a fully superconducting state to a normal state above H_{c2}.

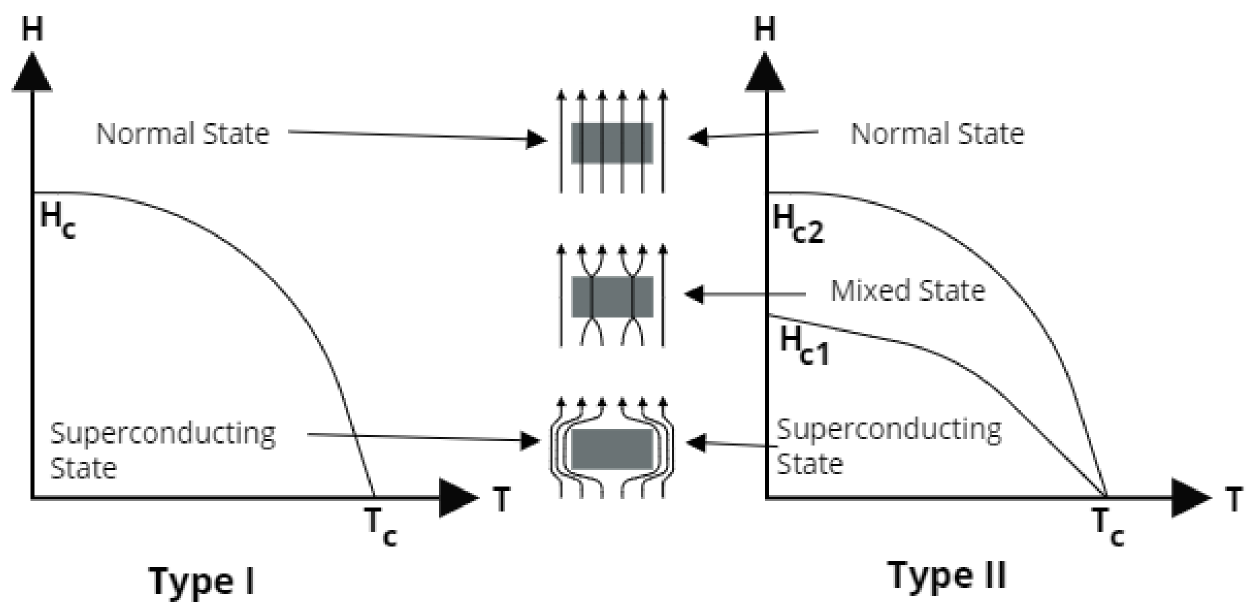

Figure 1.1. Phase Diagram of Type I and Type II Superconductors

The general behaviors of Type I and Type II superconductors are shown in Figure 1.1. From this figure, it can be seen that the critical field in a superconductor decreases as the temperature increases. Both types have a superconducting state and a normal state. If the material is below the critical temperature T_c and the external field is below H_c (H_{c1} for Type II superconductors), then the Meissner effect can be seen and the field inside the superconductor is zero. Above the critical temperature or critical field, the material does not display superconductive behavior and the external field can pass through the material. However, Type II superconductors also have the mixed state as a transition from a superconducting state to the normal state. This occurs below the critical temperature and between the critical fields H_{c1} and H_{c2}. In the mixed state, magnetic flux begins to enter the material and continues until the upper critical field is reached and the material is no longer superconducting. The magnetization curves of ideal superconducting materials are shown in Figure 1.2. Since $\mathbf{B} = \mu_0(\mathbf{H} + \mathbf{M})$, in the superconducting state $\mathbf{M} = -\mathbf{H}$ in order to have $\mathbf{B} = 0$ inside the material. In Type I superconductors, after the applied field exceeds H_c, the material enters a normal state, so $\mathbf{M}$ goes to zero. In the type II superconductor, once the applied field is greater than H_{c1}, magnetic flux starts to enter the material and the magnitude of $\mathbf{M}$ decreases until the applied field reaches H_{c2} and the material enters the normal state.

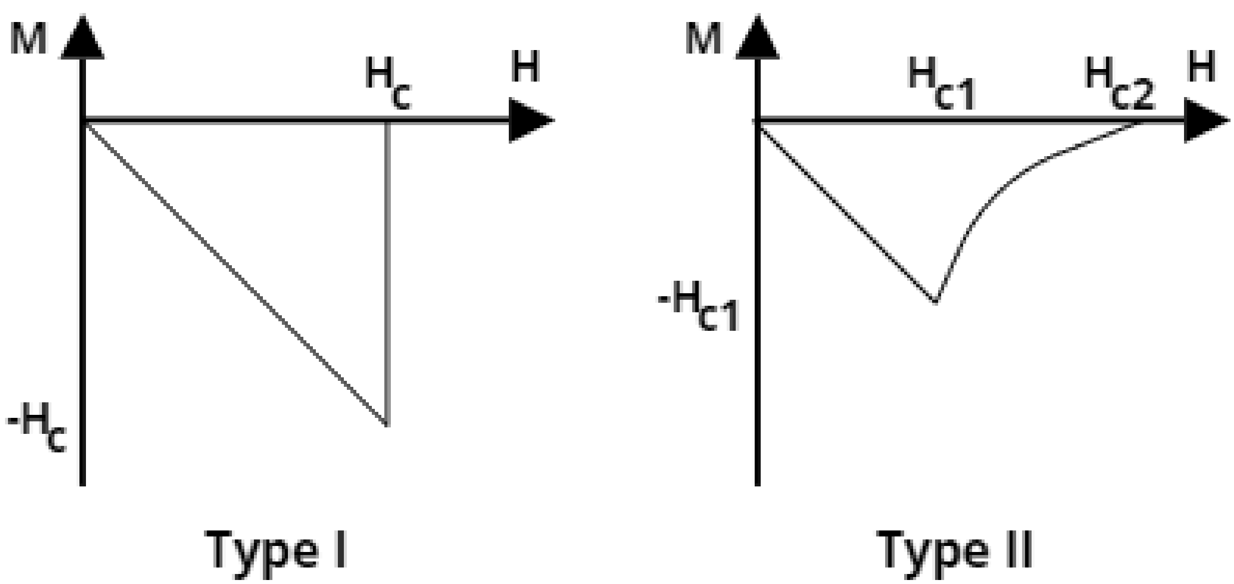

Figure 1.2. Magnetization Curves of Ideal Type I and Type II Superconductors

In [19], Abrikosov determined that the sites within the superconductor where magnetic flux penetrates (also called normal cores), occur periodically throughout the material. Due to the fact that currents circulate around these normal cores and the currents set up forces to repel one another, the normal cores distribute to form a lattice. For an ideal Type II superconductor, these normal cores are able to redistribute throughout the material and form a regular lattice. However, in practical materials there are defects that cause the magnetic flux to enter the material at fixed locations. This phenomenon is often referred to as flux pinning. In [20], Bardeen and Stephen show that for Type II superconductors in the mixed state, these flux lines or vortices may become unpinned by transport currents. It is also shown in [20] that even in mostly pure materials, unpinned vortices moving throughout the superconductor experience a viscous drag force that results in a nonzero resistance in the material, which is undesirable. According to [21], AC loss occurs in a superconductor in the presence of a varying magnetic field due to the movement of magnetic flux lines, which results in resistive loss. However, this resistance is nonlinear, and the AC loss in a superconductor is typically referred to as hysteresis loss.

Although for superconducting behavior, flux pinning is undesirable, it was recognized that flux pinning can be utilized to create magnet-type properties. Specifically, once the pinning sites are established, the currents that are present will remain (although change direction) after the external field has been removed. For this reason YBCO has been considered for use as a trapped field magnet (TFM). Indeed, in recent research it has been shown that very high fields can be trapped in HTS materials. In 2003, Tomita and Murakami were able to produce a YBCO TFM with a trapped field of 17.24 T at a temperature of 29 K [22]. In 2018, researchers improved upon this using stacks of HTS tape [23]. These tapes consist of multiple layers, and a large fraction of their volume is metallic, to improve mechanical strength. They were able to trap 17.7 T at 8 K.

To utilize magnet-type behavior, Type II superconductors are often manufactured in a manner that deliberately introduces inhomogeneities into the material to fix the magnetic flux lines or vortices in place and prevent motion. There has been much research in the area of improving the flux pinning ability of YBCO and other superconducting materials. In [24], researchers were able to introduce non-superconducting compounds into the YBCO matrix and were successful in introducing artificial pinning centers in the YBCO that increased the critical current density over that of pure YBCO. In [25], researchers attempted to introduce flux pinning sites by doping the YBCO with different atoms, using the same conditions as used in making pure YBCO. However, they found that the doped YBCO only performed as well or in some cases worse than pure YBCO. However, even in these materials, the flux pinning sites can move, resulting in the decay of the trapped field with time. In [26], Kim et al. showed a logarithmic decay of the trapped field. In [23], after the stacks of HTS tapes were magnetized, the creep rates were measured at different temperatures, and a logarithmic decay was observed. It was observed that at low temperatures (8 K and 15 K) the creep rate was minor, with a decrease of less than 0.1% of the original field in the first 30 minutes following magnetization. The creep rate was observed to increase with temperature. Specifically the trapped field in a TFM at 77.4 K was observed to decay to nearly 90% of its original field after just 1000 seconds. However, in [27], it was shown that the creep rate can be significantly reduced in TFM applications by reducing the temperature a few degrees after magnetization. Thus, flux creep is not considered a significant issue in the application of YBCO in this research.

1.3 Applications of YBCO

YBCO is used in a variety of applications as a superconductor. However, the material is brittle and is difficult to produce as a single crystal, which shows the best superconducting properties. Thus it is typically manufactured as part of a tape, in which a thin layer of YBCO or other high temperature superconductor is used as a coating on a metallic substrate. An example of such a coated conductor is SuperPower's 2G HTS wire shown in 1.3. The tape is a flexible material that can be manufactured in long lengths. In [1], SuperPower developed a tape with a thinner substrate layer and were able to produce tapes with higher critical current densities with a total tape thickness of less than 0.1 mm. In this paper, HTS tapes with widths of 2, 3, and 4 mm achieved critical currents (I_c) of 75, 110, and 144 A respectively, at a temperature of 77 K with no external field applied.

Using HTS tapes similar to that shown in 1.3, a 30 meter long 275 kV, 3 kA power cable was developed in [2]. The cable was made using two layers of YBCO tapes wrapped around a stranded copper conductor surrounded by shielding and insulation layers and a cryostat

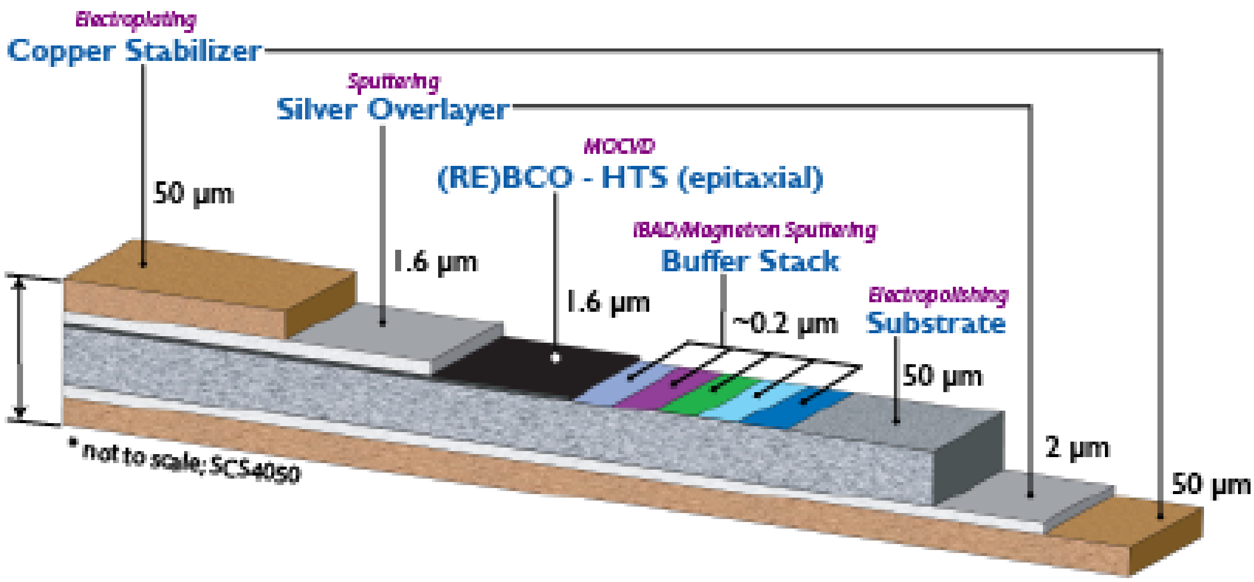

Figure 1.3. SuperPower 2G HTS Wire. From http://www.superpower-inc.com/content/2g-hts-wire.

pipe to maintain a temperature of 77 K in the conductor. With all of these layers, the cable had a total diameter of 150 mm. The design targets for this cable were to have 3 times the capacity and 1/4 to 1/5 of the loss (with cooling system included) of the conventional 275 kV power cables they were intended to replace. The critical current of the conductor layer in this cable was 6440 A at 77 K. The normalized AC loss in the HTS tape layers at 3 kA was 0.235 W/m and 0.124 W/m for conductors formed using 46 and 61 3 mm-width tapes in parallel, respectively.

Another application of YBCO is in magnetic resonance imaging (MRI) systems. MRI systems require a strong, uniform magnetic field of 1.5 T or higher [28], over a large area due to the need to provide imaging of the entire body. Due to these requirements, MRI machines commonly use superconductors to generate the magnetic field. However, these MRI magnets typically used low temperature superconductors (LTS), which have a very low critical temperature and require large amounts of liquid helium to provide cooling. In 2015, MRI systems accounted for 20% of helium usage worldwide, and in 2016 in the United States, the helium usage due to MRIs was at 30% [29]. However, in [30] YBCO conductors were used to create the coils to generate a 1.5 T field for a MRI system. The advantage of using

YBCO is that it is a HTS and requires much less cooling. Therefore, in [30] the magnet was designed to be cooled by conduction using a cryocooler rather than using a liquid helium refrigerant in the MRI system.

YBCO magnets have also been used in magnetic levitation (maglev) train systems. A prototype maglev vehicle was developed in [12], consisting of four 1.5 meter wagons on a 200 meter-long track. Bulk YBCO was used in the vehicle and was placed above a permanent magnet guideway to provide the levitation. In a static position, the YBCO provided 2000 N of levitation force, and decreased a small amount after some time due to flux creep. However, during a dynamic test with three degrees of movement (vertical, lateral, and rotational) the levitation force was observed to decrease by a much larger amount. For the test conditions used, while likely more extreme than would be seen in normal operation, it was estimated that the levitation force of the maglev vehicle would decrease by 35% after one day of operation. In [13], another maglev using YBCO magnets for levitation was designed. However, in this design, rather than cooling the YBCO in the presence of the magnets (field-cooled or FC), zero-field-cooling (ZFC) was used to cool the YBCO prior to being exposed to an external field. In this experiment, ZFC YBCO magnets were used in an attempt to reduce loss and therefore reduce the decay in levitation force. Using this method, the ZFC vehicle was observed to have lower losses from oscillations in its movement and it showed higher levitation forces.

Another popular application of YBCO is in electric machines, both as superconducting coils and as trapped field magnets. In [3] and [4], a 15 kW and 7.5 kW synchronous motor respectively, were constructed using superconducting coils made from YBCO tape. In the 15 kW motor, the stationary field winding was used, but in the 7.5 kW motor, the YBCO field coils were on the rotor. Several reluctance motors containing bulk YBCO material were constructed and tested in [7]. A synchronous linear motor was developed in [8] using bulk YBCO magnets in the secondary mover, which levitated over the stationary primary.

One of the main challenges of using YBCO TFMs is the magnetization process. There are several ways of accomplishing this, including field cooling and zero-field cooling as previously mentioned, as well as pulsed field magnetization, in which the TFM is activated by applying the external field as a series of pulses. An axial flux motor with YBCO TFMs was constructed and tested in [6] using both FC and ZFC techniques to activate the TFMs. The ZFC method was observed to have better results, with nearly 5 times the torque as the FC method. A 450 kW axial flux motor was designed in [5] which used YBCO TFMs as well as superconducting coils to magnetize the YBCO. A synchronous motor was tested in [9] that used bulk YBCO TFMs on the rotor as well as HTS coils in the stator. The rotor was magnetized using PFM with 2 magnetizing coils separate from the stator. In [31], rectangular stacks of HTS tape were used instead of bulk YBCO, and were magnetized using PFM to investigate their usage in motors. Another radial flux motor using bulk YBCO TFMs was designed and tested in [10]. Therein the researchers investigated different activation methods from both the existing stator windings as well as from the rotor.

The use of YBCO in electric machinery will be considered in the following chapters. Specifically, in Chapter 2 methods to model YBCO to support the design of electric machinery will be considered. Chapter 3 will discuss the construction of a thermal model that will be used to evaluate the thermal performance of the machines and ensure the YBCO is kept below its critical temperature. In Chapter 4, the YBCO models will be incorporated within a design model used to evaluate the performance of permanent magnet synchronous machines (PMSMs), and a multi-objective optimization is performed to find a set of optimal designs at multiple power levels. These results are then compared with similar optimizations for standard PMSMs to determine power levels where the use of YBCO within a synchronous machine may be warranted.

2. MODELING A YBCO-BASED MACHINE

In the previous chapter, some applications of YBCO were discussed, namely the use of YBCO as a trapped field magnet in electric machinery. In these machines, bulk YBCO material was used as TFMs in place of the permanent magnets that would typically be used in electric motors. In Chapter 4 a multi-objective optimization will be considered for machines that utilize YBCO TFMs. In this chapter a model will be derived that supports performance evaluation of such machines.

2.1 Machine Geometry

The geometry of the machine that will be evaluated is shown in Figure 2.1. The geometry used for this machine is based on the design of a permanent magnet synchronous machine (PMSM) in Chapter 9 of [32]. Figure 2.1 shows a surface-mounted PMSM that has been modified to used TFMs in place of the permanent magnets. In the center of the machine is the rotor shaft. Moving outward from the shaft is a magnetically inert region that acts as a spacer between the shaft and the rotor backiron. Since the magnetic flux flows in the backiron, this region does not need to be constructed of a magnetic material, so it can be made of a lightweight non-magnetic material to reduce the mass of a machine. The rotor backiron is constructed using magnetic steel and acts to direct the magnetic flux in the tangential direction in the regions between the YBCO magnets.

Moving outward beyond the rotor backiron is a thermally conductive ring that acts as a cryogenic cooling jacket. As discussed in the previous chapter, the YBCO material, which is attached to the exterior of this cooling region, must be kept below its critical temperature of 93 K to retain its superconducting properties. The cooling system and the thermal model of the machine are explained in more detail in the next chapter. Continuing outward from the YBCO is the air gap between the rotor and stator. The next region after the airgap is the stator teeth and slots, and then the outer region of the machine is the stator backiron. The stator teeth and backiron are made of a magnetic material to direct the magnetic flux. Slots are cut out of the stator material between the teeth in which the conductors that make up the windings are placed.

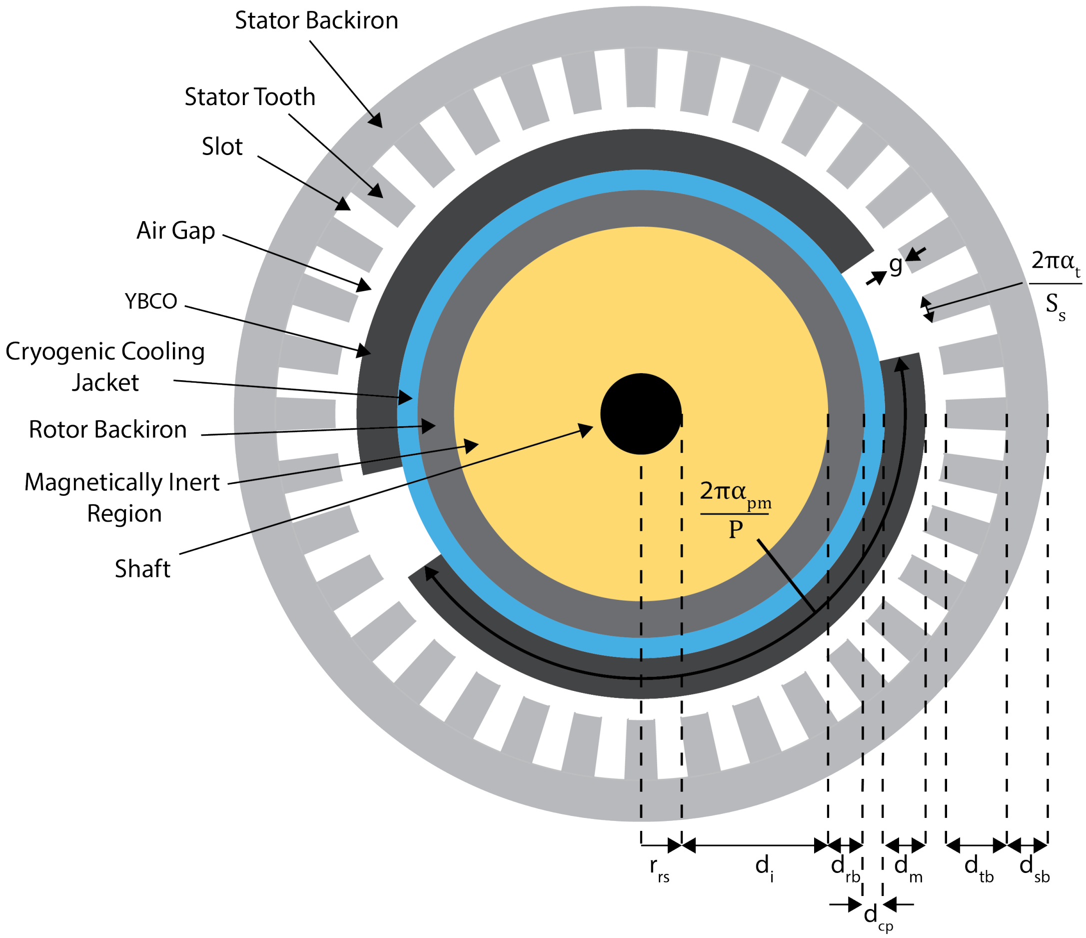

Figure 2.1. Geometry of YBCO-Based Machine

This figure shows the input design parameters that are necessary to calculate the dimensions of the machine. They include: r_{rs}, the rotor shaft radius, d_i, the depth of the magnetically inert region, d_{rb}, the rotor backiron depth, d_{cp}, the depth of the cooling plate, d_m, the depth of the TFM, g, the airgap, d_{tb}, the depth of the tooth base, and d_{sb}, the depth of the stator backiron. Also shown are α_{pm} and α_t, which define the magnet and tooth fractions, respectively. The magnet fraction α_{pm} describes the angular fraction of one pole that the magnet occupies, where P is the number of poles. Similarly, α_t is the fraction of one tooth/slot that is occupied by the tooth, where S_s is the number of stator slots.

2.2 Electromagnetic Analysis Using 2D Method of Moments

The magnetic field analysis of this machine is performed using a two-dimensional Method of Moments (MoM) formulation [33]. The Method of Moments is a numerical method used to solve electromagnetic field problems, similar to a Finite Element Analysis (FEA), with the primary difference being that MoM is used to solve integral equations rather than the differential equation form used as a basis for FEA. Typically, forming the system of equations required to solve the MoM problem would require these integral equations to be evaluated numerically. However, in [34] an analytical solution was found for the integral equation used in a 2D Galerkin MoM formulation. This paper provides a closed form for the solution of the tangential magnetic field along a line element due to a sheet current. These results were used in [35] to develop a system of equations for a 2D Galerkin MoM formulation. This system of equations expresses the total tangential magnetic field along an element due to contributions from free current sources as well as the magnetization of other elements.

2.2.1 MoM System of Equations

In [33] these results are extended to be used in the analysis of electric machines. In this paper the previous system of equations is used with the addition of the contribution of permanent magnet sources to the total magnetic field. The system of equations for the total tangential field in all of the elements is written in matrix form as

$$\mathbf{B_{tan,tot}} = \mathbf{f_{BM}}\mathbf{M_{tan}} + \mathbf{f_{BI_f}}\mathbf{I_f} + \mathbf{f_{BI_{PM}}}\mathbf{I_{PM}} \tag{2.1}$$

The total magnetic field can also be written as

$$\mathbf{B} = \mu_0(\mathbf{H} + \mathbf{M}) = \mu_0(1 + \chi)\mathbf{H} = \mu_0\mu_r\mathbf{H} \tag{2.2}$$

using the relation $\mathbf{M} = \chi\mathbf{H}$ where $\mu_r = 1 + \chi$. Using (2.2), the total tangential magnetic field in element j can also be written as

$$\mathbf{B_{tan,tot}}(j) = \frac{\mu_0 \mu_{r,j}}{\mu_{r,j} - 1}\mathbf{M_{tan}}(j) \tag{2.3}$$

or in matrix form,

$$\mathbf{B_{tan,tot}} = \mathbf{f_{B_{tot}M}} \mathbf{M_{tan}} \tag{2.4}$$

Equating (2.1) and (2.4), $\mathbf{B_{tan,tot}}$ can be eliminated and the system of equations is rearranged and written as

$$[\mathbf{f_{B_{tot}M}} - \mathbf{f_{BM}}]\,\mathbf{M_{tan}} = \mathbf{f_{BI_f}}\mathbf{I_f} + \mathbf{f_{BI_{PM}}}\mathbf{I_{PM}} \tag{2.5}$$

where $\mathbf{M_{tan}}$ is an $N \times 1$ vector of the unknown tangential magnetizations of each element, $\mathbf{I_f}$ is an $N_f \times 1$ vector of free current sources from the stator windings, and $\mathbf{I_{PM}}$ is an $N_{PM} \times 1$ vector of permanent magnet sources. For the analysis of a PMSM or another machine with permanent magnets, a magnet magnetized in the radial direction is represented by sheet current sources placed along the magnet sides. In [33], these permanent magnet sources were determined to be:

$$\mathbf{I_{PM}} = \frac{-B_r}{\mu_0 \mu_{r,rec}} l_{PM} \tag{2.6}$$

where B_r is the residual flux density of the magnet, $\mu_{r,rec}$ is its relative permeability, and l_{PM} is the side length of the magnet. However, in this machine TFMs are used rather than permanent magnets, so this term must be modified in a YBCO-based machine. A method for calculating the current sources in a TFM is discussed in Section 2.3. The system of equations used for the analysis of the YBCO machine is the same as (2.5), except $\mathbf{f_{BI_{PM}}}$ and $\mathbf{I_{PM}}$ are replaced by the matrices $\mathbf{f_{BI_{TFM}}}$ and $\mathbf{I_{TFM}}$.

A single pole of the mesh used in the MoM analysis of a PMSM machine is shown in Figure 2.2. In the MoM analysis, only the active material is meshed. Thus, it can be seen here that only the rotor and stator steel and the permanent magnet material are included in the mesh. Also, for MoM analysis where the materials are magnetically linear, only the

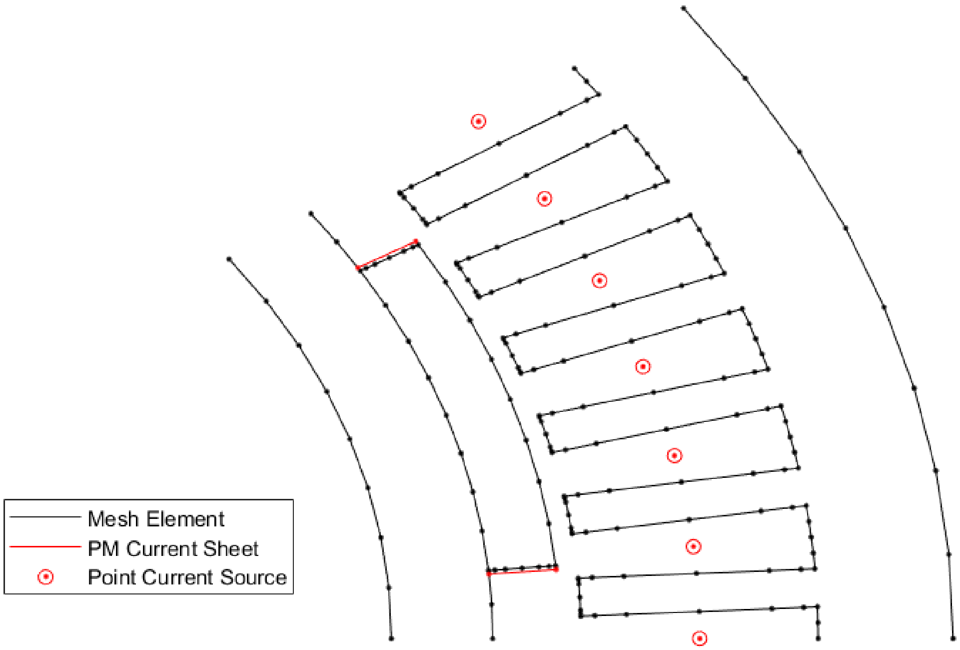

Figure 2.2. Mesh of PMSM used in MoM analysis

surface of the material is meshed [33]. These mesh elements are shown by the black line segments and the points are nodes between elements. The current sheets for the permanent magnet source are shown by the two red lines. The free current sources from the stator windings are shown in each of the stator slots. They are represented by a single point current source located at the center of each slot.

2.2.2 Constructing MoM Matrices

As can be seen from (2.3) and (2.4), $\mathbf{f_{B_{tot}M}}$ is an $N \times N$ diagonal matrix relating the magnetic field in each element to its magnetization, and its entries are calculated as

$$\mathbf{f_{B_{tot}M}}(i,i) = \frac{\mu_0 \mu_{r,i}}{\mu_{r,i} - 1} \tag{2.7}$$

In order to calculate $\mathbf{f_{BM}}$, it is first divided into two $N \times N$ square matrices such that $\mathbf{f_{BM}} = \mathbf{f_{BI}}\mathbf{f_{IM}}$. The matrix $\mathbf{f_{IM}}$ is a diagonal matrix relating the magnetization of each element to its bound current with $\mathbf{I_b} = \mathbf{f_{IM}}\mathbf{M_{tan}}$. The diagonal entries of this matrix are $\mathbf{f_{IM}}(i,i) = -l_i$, where l_i is the length of the line element. The $\mathbf{f_{BI}}$ matrix relates the magnetic field in element j due to a bound sheet current in element i, and $\mathbf{f_{BI_{PM}}}$ is calculated in the same manner. Similarly, $\mathbf{f_{BI_f}}$ relates the magnetic field in element j due to a current source i, where the current source is a filament rather than a sheet. These matrices are given in [33] using the closed-form solutions to the integration over the observation element that were derived in [34] and are repeated below.

For an observation element j with endpoints $(x_{1,j}, y_{1,j})$ and $(x_{2,j}, y_{2,j})$ and a filamentary current source i located at (x_{I_f}, y_{I_f}):

$$\mathbf{f_{BI_f}}(j,i) = \frac{\mu_0}{2\pi l_j}\left(\tan^{-1}\left(\frac{x'_{2,j} - x'_{I_f}}{y'_{I_f}}\right) - \tan^{-1}\left(\frac{-x'_{I_f}}{y'_{I_f}}\right)\right) \tag{2.8}$$

where the coordinates have been transform to the observation reference frame as indicated by the prime notation. This geometry is shown in Figure 2.3(a). In the case that the source is a sheet current as in Figure 2.3(b), the elements of the $\mathbf{f_{BI}}$ matrix are computed by:

$$\mathbf{f_{BI}}(j,i) = -\frac{\mu_0}{2\pi l_2 l_1^2}\begin{pmatrix} \mathbf{l_1}\cdot\mathbf{l_2}\,\mathrm{atan2}^*(\mathbf{l_5}\times_\mathbf{2}\mathbf{l_6}, \mathbf{l_5}\cdot\mathbf{l_6}) \\ +\mathbf{l_1}\cdot\mathbf{l_3}\,\mathrm{atan2}^*(\mathbf{l_5}\times_\mathbf{2}\mathbf{l_3}, \mathbf{l_5}\cdot\mathbf{l_3}) \\ +\mathbf{l_1}\cdot\mathbf{l_4}\,\mathrm{atan2}^*(\mathbf{l_4}\times_\mathbf{2}\mathbf{l_6}, \mathbf{l_4}\cdot\mathbf{l_6}) \\ +\mathbf{l_1}\times_\mathbf{2}\mathbf{l_2}\ln^*(l_6/l_5) \\ +\mathbf{l_1}\times_\mathbf{2}\mathbf{l_3}\ln^*(l_3/l_5) \\ +\mathbf{l_1}\times_\mathbf{2}\mathbf{l_4}\ln^*(l_6/l_4) \end{pmatrix} \tag{2.9}$$

where the vectors $\mathbf{l_1}$ and $\mathbf{l_2}$ are the source and observation elements, respectively, and $\mathbf{l_3} - \mathbf{l_6}$ are the vectors formed between their endpoints. The $\times_2$ operator is a 2D cross product and the starred operators are defined as

$$\begin{aligned} \mathrm{atan2}^*(\alpha, \beta) &= \left\{ \begin{array}{cc} \frac{\pi}{2} & \alpha = \beta = 0 \\ \mathrm{atan2}(\alpha, \beta) & else \end{array} \right\} \\ \ln^*(\alpha) &= \left\{ \begin{array}{cc} 0 & \alpha = 0, \alpha \to \infty \\ \ln(\alpha) & else \end{array} \right\} \end{aligned} \tag{2.10}$$

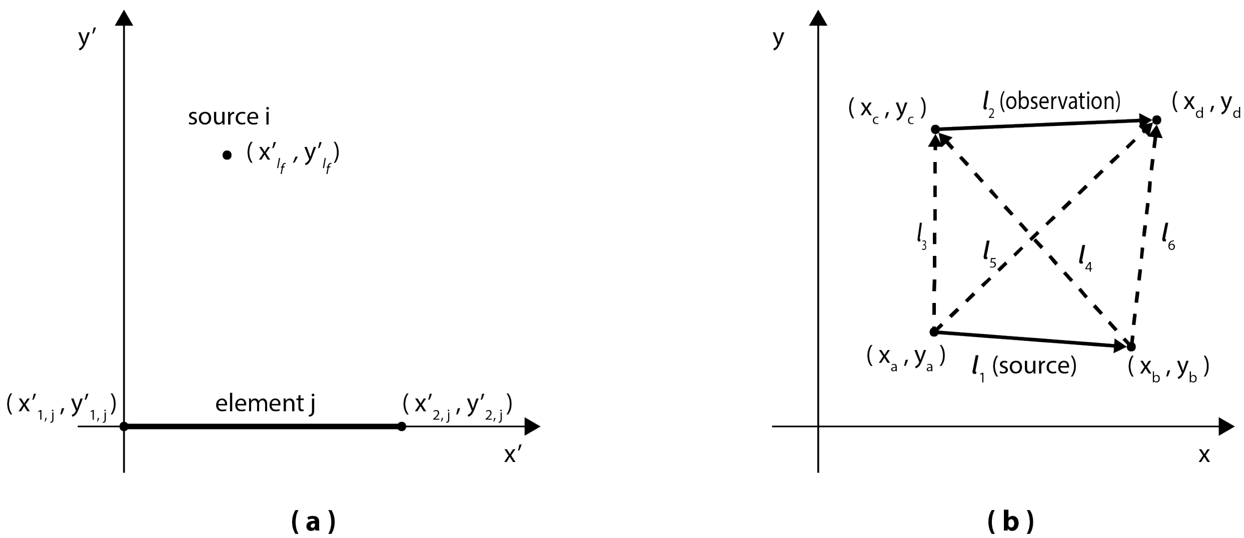

Figure 2.3. Geometry used in the calculation of $\mathbf{f_{BI_f}}$ and $\mathbf{f_{BI}}$ matrix entries

2.2.3 Postprocessing

In addition to solving for the magnetic field in the mesh elements used in the MoM analysis, there are several other quantities of interest that are desired in order to analyze a particular design. Two examples are the inductances and electromagnetic torque. Methods to calculate these quantities using the the MoM analysis have been developed and are discussed in this section.

Inductance Calculations

The inductances of the windings are desired in order to evaluate the performance of the machine. In [36], a method to calculate inductances using 2D MoM was derived. This method calculates the partial inductance between two sheet currents or two filamentary currents. This method was extended for use in calculating the inductances in electric machines in [37]. In electric machines there are commonly three types of partial inductance calculations: partial mutual inductance between a sheet current and a filamentary current, partial self inductance of a filamentary current, and the partial mutual inductance between filamentary currents. The first case is between a bound sheet current and a conductor, and the sheet to filament partial inductance is given in [37] as

$$L_{pm\cdot|} = -\frac{\mu_0}{4\pi w_2}\begin{pmatrix} (x_{22}^L - x_1^L)\ln\left((x_{22}^L - x_1^L)^2 + (y_1^L)^2\right) \\ +2y_1^L\tan^{-1}\left(\dfrac{x_{22}^L - x_1^L}{y_1^L}\right) \\ -(x_{21}^L - x_1^L)\ln\left((x_{21}^L - x_1^L)^2 + (y_1^L)^2\right) \\ -2y_1^L\tan^{-1}\left(\dfrac{x_{21}^L - x_1^L}{y_1^L}\right) \end{pmatrix} \tag{2.11}$$

where the L superscript refers to an alternate reference frame that was used to simplify the calculation. In this reference frame the filament located at (x_1, y_1) is a point on the y-axis, and the sheet with endpoints at (x_{21}, y_{21}) and (x_{22}, y_{22}) is located along the x-axis. The partial self and mutual inductances between filaments are given by

$$L_{ps\cdot} = \frac{\mu_0}{8\pi} - \frac{\mu_0}{2\pi}\ln(r_w) \tag{2.12}$$

$$L_{pm\cdot\cdot} = -\frac{\mu_0}{2\pi}\ln(d) \tag{2.13}$$

respectively, where r_w is the conductor radius and d is the distance between the two filaments. In (2.11)-(2.13), the pm and ps subscripts refer to a partial mutual or partial self inductance, respectively. The $\cdot$ and $|$ subscripts denote a filamentary element and a sheet element, respectively.

Using these expressions, the inductances in an electric machine can be calculated using the partial inductances between all of the current sources in the MoM analysis. This method is then applied in [37] to calculate the inductances in a 3-phase electric machine with distributed windings. In a distributed winding the conductors are grouped into multiple coils and the winding is distributed over several slots rather than being concentrated in one spot. For the inductance calculations, the conductors for different phases are kept separate, but all of the conductors in a slot that are part of the same winding are represented as a single filament. In order to determine the inductance L_{asas}, the a-phase winding is excited with no current in the phase b and c windings, and then the total flux linking all of the a-phase coils is calculated. Then L_{asas} can be calculated by $L_{asas} = \lambda_{as}/i_{as}$.

The flux linking the first coil, $as1$, has contributions from all of the bound sheet currents as well as all of the free currents in the other a-phase conductors. In this calculation a free space inductance is used, which was defined as the inductance calculated from the flux linkage due to a single current element, with all of the other free and bound currents set to zero. The contribution from bound currents is given by

$$\mathbf{L}^{fs}_{as,b}(i) = L_{pm\cdot|}(x^{L_1}_{21}, x^{L_1}_{22}, x^{L_1}_{1}, y^{L_1}_{1}) - L_{pm\cdot|}(x^{L_2}_{21}, x^{L_2}_{22}, x^{L_2}_{1}, y^{L_2}_{1}) \tag{2.14}$$

for each of the bound currents $i = 1...N$. The L_1 superscript indicates the reference frame of the current sheet and the $as1'$ side of the coil (coil current into page), and the L_2 superscript indicates the reference frame of the current sheet and the $as1$ side of the coil (coil current out of page). The contributions from free current sources are calculated using

$$\mathbf{L}^{fs}_{as,f}(j) \begin{cases} L_{pm\cdot\cdot}(d_{as1'}) - L_{pm\cdot\cdot}(d_{as1}) & \forall j \neq j_{as1'}, j_{as1} \\ L_{ps\cdot}(r_w) - L_{pm\cdot\cdot}(d_{as1'}) & j = j_{as1'} \\ L_{pm\cdot\cdot}(d_{as1}) - L_{ps\cdot}(r_w) & j = j_{as1} \end{cases} \tag{2.15}$$

for each free current $j = 1...N_f$. In this equation $d_{as1'}$ and d_{as1} are the distances from the free current to the respective coil side.

From the above two equations the total flux linking the coil is

$$\lambda_{as1} = N_{as1} \left(\left[\mathbf{L}_{as,b}^{fs} \right]^T \mathbf{I}_b + \left[\mathbf{L}_{as,f}^{fs} \right]^T \mathbf{I}_f \right) \tag{2.16}$$

where N_{as1} is the number of turns in the $as1$ coil and $\mathbf{I}_b$ and $\mathbf{I}_f$ are the vectors of all of the bound and free currents. The total flux linkage for the a-phase winding in the first pole of the machine is the sum of the flux linking all of the a-phase coils in pole 1. Then the total a-phase flux linkage in a P-pole machine is

$$\lambda_{as} = \frac{P}{2} \lambda_{as,P=1} \tag{2.17}$$

This process can be repeated to calculate L_{asbs} by exciting only winding b and calculating λ_{as}. Once L_{asas} and L_{asbs} are known, all of the self and mutual inductances in the machine can be found by applying appropriate phase shifts.

Torque Calculations

Another quantity of interest in the design of this machine is the electromagnetic torque. A MoM torque calculation was derived in [38] for the contributions to the torque between individual MoM elements and current sources. In this paper, the Lorentz force $\mathbf{F} = \mathbf{I} \times \mathbf{B}$ is computed and then the torque is calculated as $\mathbf{T_e} = \mathbf{r} \times \mathbf{I} \times \mathbf{B}$, where $\mathbf{r}$ is the radius from the origin to the observation element. The geometry used for the torque on a line element by a point source is provided in Figure 2.4. The contribution to the total torque due to these two elements is given by

$$T_{|\cdot} = \frac{\mu_0 I_1 I_2}{2\pi l_2} \begin{pmatrix} \begin{pmatrix} x_a \cos(\phi_2) \\ + y_a \sin(\phi_2) \end{pmatrix} \operatorname{atan2} \begin{pmatrix} \boldsymbol{l_4} \times_2 \boldsymbol{l_6}, \\ \boldsymbol{l_4} \cdot \boldsymbol{l_6} \end{pmatrix} \\ \begin{pmatrix} -x_a \sin(\phi_2) \\ + y_a \cos(\phi_2) \end{pmatrix} \log \left(\frac{l_6}{l_4} \right) \end{pmatrix}. \tag{2.18}$$

In this equation, I_1 and I_2 are the currents in the source and observation elements, respectively, and ϕ_i is the angle that the corresponding vector l_i makes with the x-axis. The other type of torque contribution that exists in the PMSM and the YBCO-based machine is the torque on a line element from another line element source. The geometry for this calculation is the same that was used to compute the entries of $\mathbf{f_{BI}}$ as shown in Figure 2.3(b). In this equation $l_a - l_d$ are the lengths of the vectors from the origin to each of the points a-d shown in the figure.

$$T_{||} = -\frac{\mu_0 I_1 I_2}{4\pi l_1^2 l_2^2} \left(\begin{array}{l} \left(\begin{array}{c} l_1 l_2 l_2 l_c \cos(\phi_1+\phi_2-\phi_2-\phi_c) \\ +l_1 l_2 l_2 l_d \cos(\phi_1+\phi_2-\phi_2-\phi_d) \end{array} \right) \operatorname{atan2} \left(\begin{array}{c} \boldsymbol{l_5} \times_2 \boldsymbol{l_6}, \\ \boldsymbol{l_5} \cdot \boldsymbol{l_6} \end{array} \right) \\ + \left(\begin{array}{c} l_1 l_2 l_3 l_c \cos(\phi_1+\phi_2-\phi_3-\phi_c) \\ +l_1 l_2 l_3 l_a \cos(\phi_1+\phi_2-\phi_3-\phi_a) \end{array} \right) \operatorname{atan2} \left(\begin{array}{c} \boldsymbol{l_5} \times_2 \boldsymbol{l_3}, \\ \boldsymbol{l_5} \cdot \boldsymbol{l_3} \end{array} \right) \\ + \left(\begin{array}{c} l_1 l_2 l_4 l_c \cos(\phi_1+\phi_2-\phi_4-\phi_c) \\ +l_1 l_2 l_4 l_b \cos(\phi_1+\phi_2-\phi_4-\phi_b) \end{array} \right) \operatorname{atan2} \left(\begin{array}{c} \boldsymbol{l_4} \times_2 \boldsymbol{l_6}, \\ \boldsymbol{l_4} \cdot \boldsymbol{l_6} \end{array} \right) \\ \qquad - \left(\begin{array}{c} l_1 l_2 l_2 l_c \sin(\phi_1+\phi_2-\phi_2-\phi_c) \\ +l_1 l_2 l_2 l_d \sin(\phi_1+\phi_2-\phi_2-\phi_d) \end{array} \right) \log\left(\frac{l_6}{l_5}\right) \\ \qquad - \left(\begin{array}{c} l_1 l_2 l_3 l_c \sin(\phi_1+\phi_2-\phi_3-\phi_c) \\ +l_1 l_2 l_3 l_a \sin(\phi_1+\phi_2-\phi_3-\phi_a) \end{array} \right) \log\left(\frac{l_3}{l_5}\right) \\ \qquad - \left(\begin{array}{c} l_1 l_2 l_4 l_c \sin(\phi_1+\phi_2-\phi_4-\phi_c) \\ +l_1 l_2 l_4 l_b \sin(\phi_1+\phi_2-\phi_4-\phi_b) \end{array} \right) \log\left(\frac{l_6}{l_4}\right) \end{array} \right) \tag{2.19}$$

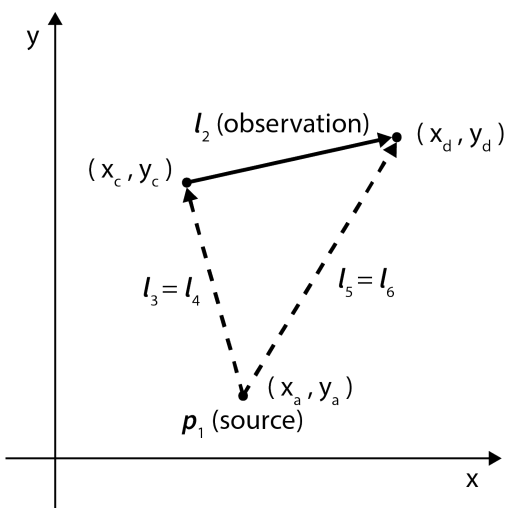

Figure 2.4. Geometry used to calculate torque on line element by point source

As in the inductance calculations, the $\cdot$ and $|$ subscripts refer to the contribution to the electromagnetic torque due to the interaction between filamentary currents and sheet currents. The total torque can be calculated for the machine using (2.18) and (2.19). The individual torque contributions are computed and summed for all of the interactions between stator current sources and rotor observation elements. In both the PMSM and the YBCO machine, there are 4 types of contributions to the total torque calculation: bound sheet currents in stator elements acting on both bound currents of the rotor steel and the bound currents in the magnet in the rotor, and stator free current (point) sources acting on the bound currents of the rotor steel and and magnets.

2.3 Calculating Currents in TFM

In order to represent the YBCO TFM within the MoM analysis, the currents induced in the material must first be calculated. In the previous chapter it was described how trapped field magnets are formed when a field greater than H_{c1} is applied to the YBCO. At this level magnetic flux begins to enter the puck and once the external field is removed some flux can remain trapped in the material at pinning sites. Since this behavior occurs on the microscopic level, it would be difficult to model efficiently throughout the entire TFM. In [39] and [40], Bean developed a theory to model the superconductor on a macroscopic level. In this theory he assumes that an applied field will induce a current with a critical current density J_c in the YBCO that flows up to a penetration depth Δ from the outer edge. In this macroscopic model, it is assumed that any applied field will cause currents to be induced and the material will be in the mixed state. In other words, $H_{c1} = 0$ in the model given by Bean in [40]. As the applied field increases, the penetration depth from the outer edge increases and the induced current flows in a larger portion of the superconductor. At a field of H^*, this current flows throughout the entire volume. If a field is applied and then subsequently removed, then it will experience an electromotive force in the opposite direction as the initially applied field and the currents will reverse direction.

The behavior of the Bean model for an external field applied to a superconducting cylinder is shown in Figure 2.5. The local field and current density in the cylinder is shown in the

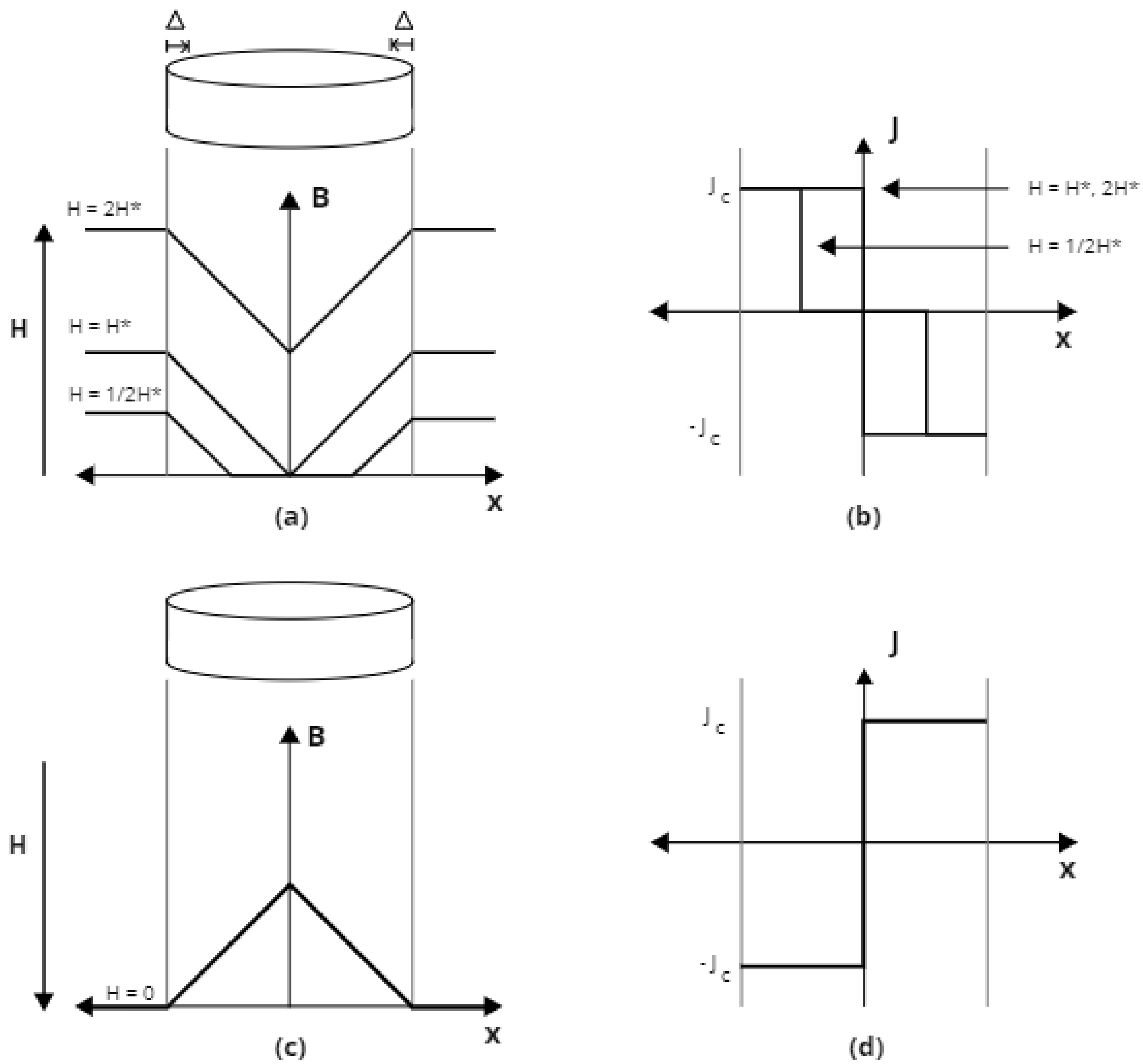

Figure 2.5. Plots of fields and current density according to the Bean model

upper two plots, Figure 2.5(a) and (b), respectively. From these two plots it can be seen that as the field is increased from 0, a current is induced starting from the outside edge of the material, and as the field increases the penetration depth increases and the current flows in a larger volume in the material. When the applied field reaches H^*, the critical current density flows throughout the entire volume, so if the external field is further increased, the current density distribution remains the same. The bottom two plots show the resulting field and current density as the applied field is reduced from $2H^*$ to 0. As the field is removed the surface currents reverse direction, and the critical current density still flows throughout the entire volume (in the opposite direction as 2.5(b)) with no applied field, as shown in 2.5(d). This results in magnetic flux becoming trapped in the material as shown in 2.5(c).

The above model proposed by Bean applies to long cylinders (height $\gg$ diameter) and thin slabs (height $\gg$ width). In many TFM applications YBCO pucks with varying geometries and depths are used, and therefore the model must be modified to accommodate for these different cases. In [41], Theuss et al. modeled a superconducting cylindrical film using concentric current loops. Using the Biot-Savart law, the contribution to the total field can be calculated and then the total field is the sum of the contributions of each current loop. In [42], Forkl investigated the field distribution of thin films. Using the previously mentioned method, a model of the **B** field could be fitted to experimental data and then the current density distribution required to produce this field was calculated. Analytical models of the field and current density distribution in thin films are given for a superconducting bar with a rectangular cross section for the case where the critical current density has fully penetrated the sample. Brandt et al. developed an analytical model for the flux density and current distribution within a thin film in a partially penetrated state in [43].

Brandt extended this model to superconducting bars of finite thickness with rectangular cross sections in [44]. This model is of most interest in this research, because it most closely represents the shape of the TFMs used in this YBCO-based machine. For a rectangular bar with a width of 2a and height 2b, the penetration field H_p (H^* in the Bean model), at which the magnetic flux penetrates the entire volume of the superconductor, is given by

$$H_p = J_c \frac{b}{\pi} \left[\frac{2a}{b} \arctan \frac{b}{a} + \ln \left(1 + \frac{a^2}{b^2} \right) \right] \tag{2.20}$$

and the sheet current density is

$$J_s(x) = \begin{cases} \dfrac{2J_c d}{\pi} \arctan \left[\left(\dfrac{a^2 - x_0^2}{x_0^2 - x^2} \right)^{1/2} \dfrac{x}{a} \right] & 0 \le x \le x_0 \\ J_c d & x_0 \le x \le a \end{cases} \tag{2.21}$$

In the above equation $d = 2b$ is the height of the bar and $x_0 = a/cosh(\pi H_a/J_c d)$ is the position along the x-axis at y=0, where magnetic flux has penetrated into the bar from the outer edge. Brandt defines this sheet current density $J_s(x)$ as

$$J_s(x) = \int_{-b}^{b} J(x, y)dy \tag{2.22}$$

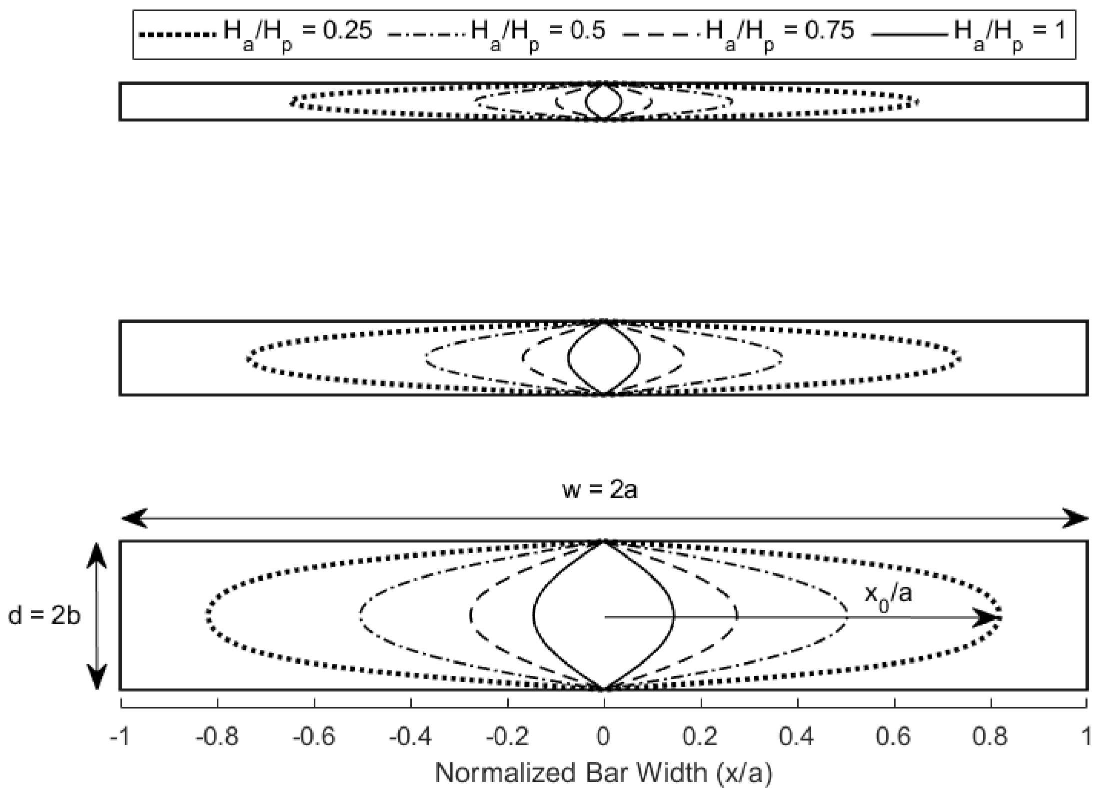

Figure 2.6. Computed Flux Fronts in Rectangular Superconducting Bar

The flux fronts calculated from this model are shown for different levels of applied field H_a for several geometries in Figure 2.6. From top to bottom, the superconducting slabs shown have height to width ratios of 0.05, 0.1, and 0.2. The plotted lines represent the portion of the material that magnetic flux has entered, and the inner region has no current flowing and B = 0 in this region. The outer portion of the bar has a current density of J_c. From these plots it can be seen that this analytical model is most accurate for thin strips. For an applied field equal to the calculated penetration field using (2.20), the model does not predict that the critical current will flow throughout the entire bar. However, as long as the TFM being modeled is not too thick, this analytical model is assumed to provide a good approximation of the current distribution.

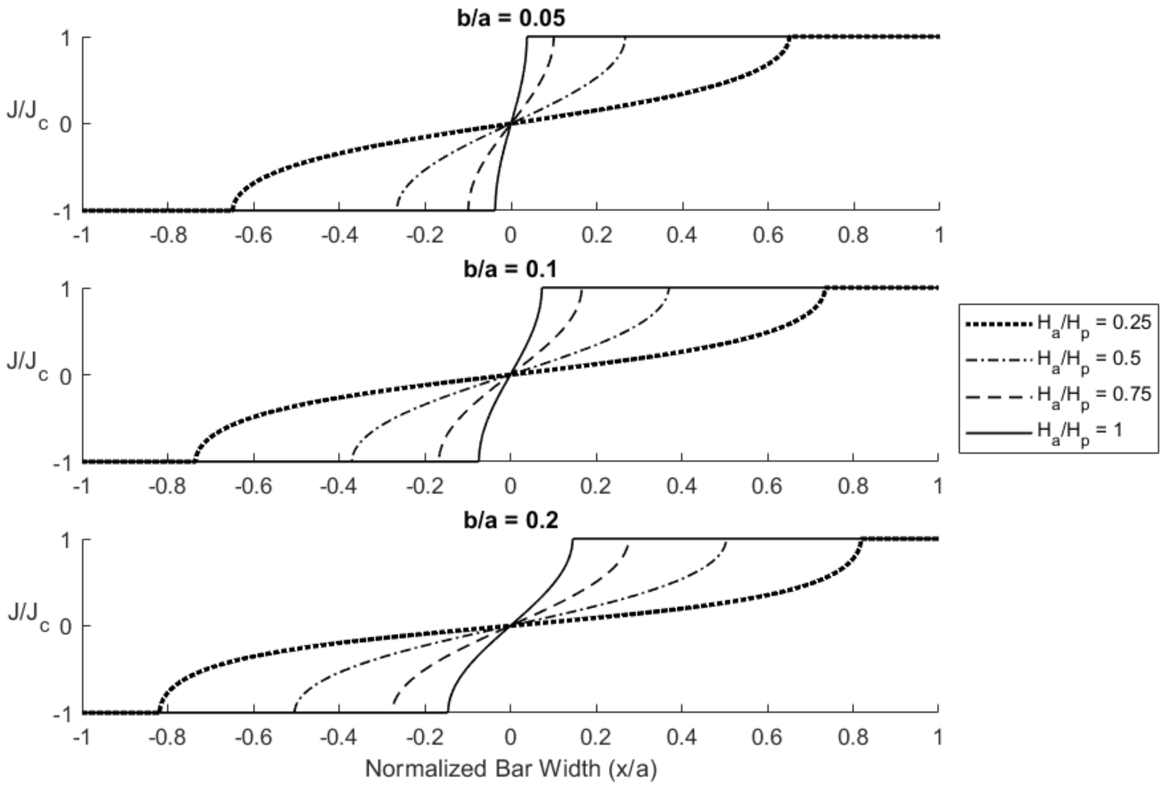

Figure 2.7. Normalized Current Density in Rectangular Superconducting Bar

The calculated current density distribution for these three bars is shown in Figure 2.7. The current distribution shown here is a sheet current density as shown by (2.21). In this calculation $J(x, y)$ is either J_c or 0. For $x \geq x_0$ the critical current density flows throughout the entire height of the bar, so the sheet current density is J_c. Moving toward the center of the bar, this model assumes that the critical current density is only present at the upper and lower surfaces of the bar as shown in Figure 2.6. As a result, the sheet current density, which is an average of $J(x, y)$ over the bar's height, decreases from J_c at $x = x_0$ to zero at the bar's center ($x = 0$).

Although the analytical method described above offers a fast solution to approximate the current density distribution in superconductors, its downside is that it only applies to simple geometries. As a result, numerical methods are often used to model superconductors instead. In the Bean model, it is assumed that if an external field is applied to the superconductor that a critical current density J_c flows in regions of the superconductor that the field has penetrated. This can be summarized using the E-J relationship that the current density is $\pm J_c$ at locations where the electric field is nonzero within the material. Some models use a power-law relationship where E is proportional to J^n with $n \gg 1$. Using this E-J relationship in superconductors, along with the electric field induced in the superconductor the current distribution was solved numerically inside a superconductor in [45]. A finite element method was used in [46] to solve Poisson's equation and calculate the currents that would be induced within the superconductor due to an external field.

In [47], a algorithm was developed by Coombs et al. to iteratively calculate the currents in a superconductor. For a two-dimensional problem, the cross section is first divided into individual elements. The magnetic vector potential is calculated and then a current density J_c is induced in the element with the maximum magnetic vector potential, and $-J_c$ in the element where A is minimum. Then A is recalculated with the addition of these induced currents and the process repeats until the end solution is achieved. This algorithm can also be used for three-dimensional problems with simple geometries, such as a cylindrical puck, since the current can be assumed to flow in circular loops.

Another method for calculating the current distribution and trapped field in TFMs is presented by Davey et al. in [48] and [49]. In this method a disk-shaped TFM is split into cells, each of which is capable of carrying a critical current $i_c = J_c \cdot A$, where A is the cross-sectional area of the cell. Then using the mutual inductance coupling between cells, and from the source coil to the cells, the currents in each of these cells is calculated, and the critical current i_c is placed in the cell with the maximum current greater than i_c. This is repeated until all of the cells have the critical current flowing in them or none of the remaining cells have calculated currents greater than i_c.

In this research, the TFM analysis is to be used in an optimization with a genetic algorithm. It is expected that a large number of design candidates will be evaluated over many generations. It is common for hundreds of thousands of designs to evaluated over the course of the optimization. Therefore, the analytical model presented by Brandt in (2.20) and (2.21) was used since this model can provide a reasonable estimate of the current distribution in the TFM with only a few straightforward calculations. Also, since the TFMs that will be used in this analysis will have trapped fields of a few Tesla, it can be assumed that the TFMs are fully activated and have the maximum achievable trapped field. In the case that the TFM is fully activated the critical current density has penetrated the entire sample so the current distributions calculated by the different models are not assumed to differ significantly.

As previously mentioned, the TFMs used in this analysis are assumed to have fields of several Tesla trapped, so it may be assumed that the applied field H_a is greater than the penetration field H_p. Therefore, for this TFM analysis it was assumed that the applied field would be sufficiently large that the current distribution in the YBCO after this field is removed follows the solid line in Figure 2.7 corresponding to $H_a/H_p = 1$. According to the Bean model as illustrated in Figure 2.5, this would require an applied field of twice the trapped field. However, others have since shown that the peak trapped field can be achieved with considerably lower applied fields [50].

In [51], the authors were successfully able to produce 53 YBCO TFMs with an average trapped field of 2.04 T at a temperature of 77 K. The TFMs used were cylindrical pucks with a 20 mm diameter and a height of 8 mm. In order to compare the results of the analytical 2-dimensional model with experimental results, a TFM with the same cross-section was represented using the 2D MoM, recognizing the fact that the rectangular shape used in the MoM analysis will yield different results than the cylindrical puck. For implementation within the 2D MoM analysis, the TFM was represented as sheet current elements distributed throughout the material. The placement of the sheet currents throughout the puck is shown in Figure 2.8. For this example the TFM was represented using 16 current loops, or 32 current sheets, with the direction of current along these elements either into or out of the page ($\pm z$ direction).

Using Brandt's model, (2.21) was used to calculate the current density distribution throughout the width of the YBCO TFM, assuming $H_a/H_p = 1$. Then from this continuous current distribution, a sheet current density was assigned to each sheet current element by averaging the current density over each region and multiplying by its width. The current density distribution was initially calculated with $J_c = 1\ A/m^2$, and then the field at the surface of the TFM was calculated. The maximum of this trapped field was found and then scaled in order to achieve the desired trapped field in the TFM (2 T in this example). This was then used to determine J_c and the magnitude of the sheet currents required to produce the desired field. The sheet currents are calculated by integrating the volume current density distribution in the puck over the width of each region containing a current sheet. The sheet currents that were calculated for this example are plotted on the right axis in Figure 2.8.

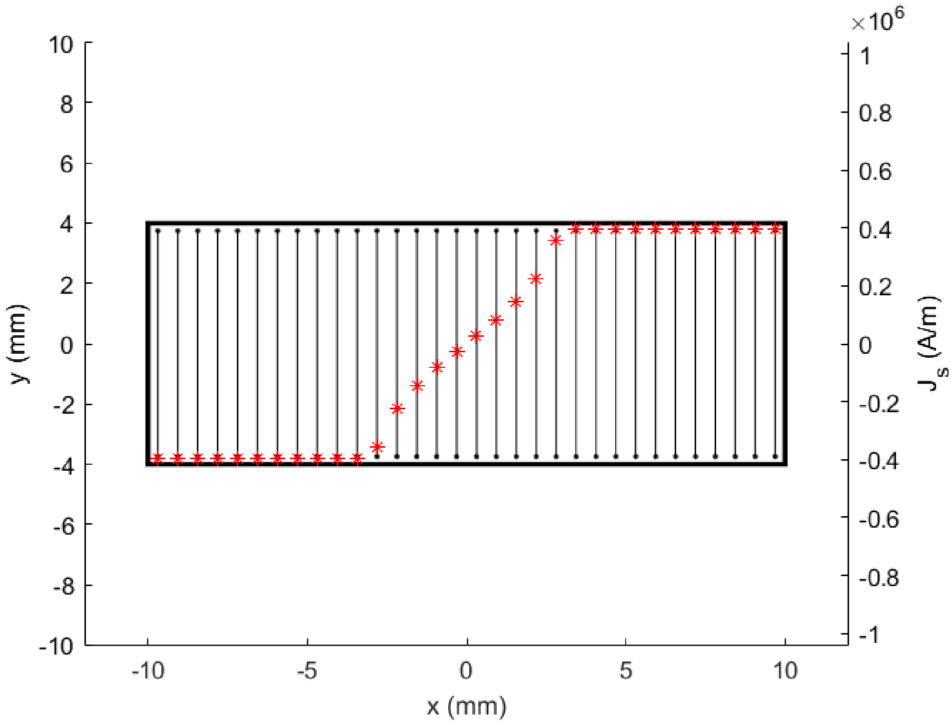

Figure 2.8. Placement of current sheets in TFM

The resulting field from this current distribution is shown in Figure 2.9. The B shown is the field in the y-direction, calculated at the TFM surface (y = 4 mm). The critical current does not flow throughout the entire volume when using (2.20) and (2.21), as can be seen in Figure 2.7. The resulting field does not exactly match that predicted by the Bean model as shown in Figure 2.5(c), but rather has a more rounded peak. However, Figure 9 in [51] shows a 3D plot of the field measured from one of the TFM samples in this production run.

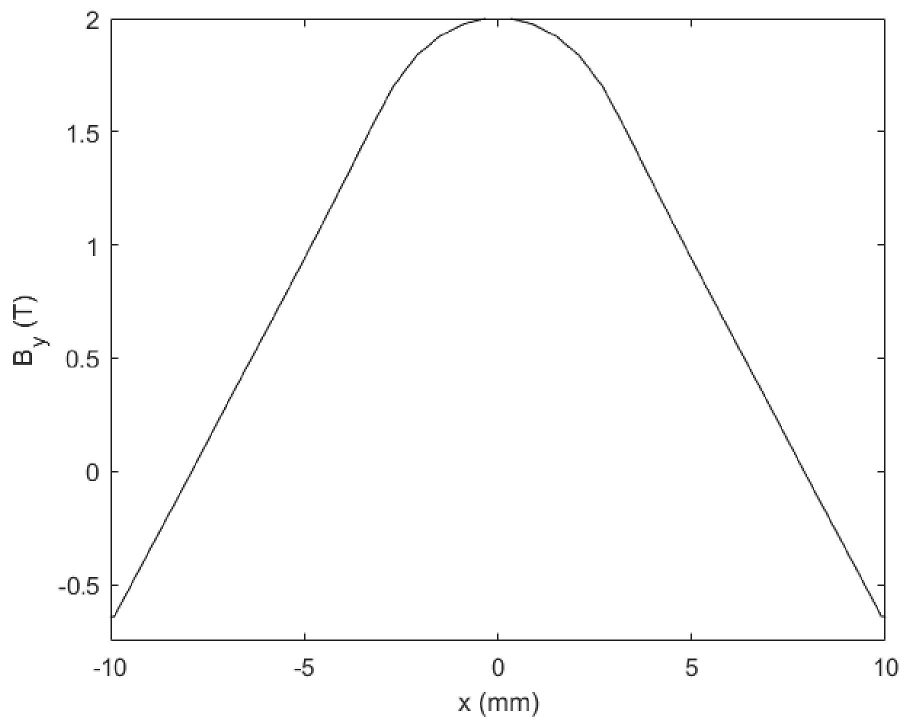

Figure 2.9. Calculated field at surface of 2 T TFM

It can be seen that the field calculated using the analytical model in the 2D MoM produces a reasonable match to the experimental results in [51].

The calculated critical current density required to produce this 2 T TFM is 63.4 kA/cm^2. However, in [50], these authors performed experiments on pulsed activation of the TFM using the same puck geometry. In this paper they report critical current densities around 50 kA/cm^2 for pucks of the same geometry as those used in [51] with a maximum trapped field around 2.2 T. The difference seen in using the Brandt model is likely due to the fact that in the 2D MoM representation, it is assumed the current flows in infinitely long sheets as opposed to circular loops likely encountered in the experimental YBCO pucks. In [50] the authors produced a TFM with a trapped field of 2.75 T at its surface. However, they estimated that only 88% of the maximum flux was trapped and if the puck was to be fully activated they calculated a trapped field of 3.13 T at the surface. To accomplish a 3 T TFM using the same geometry and activation level as shown in Figure 2.9, the calculated critical density would also increase by a factor of 50% to about 95 kA/cm^2, which is roughly double the maximum critical current density reported by these authors. As was previously mentioned, the 2D MoM representation may require a larger current to produce the same field in the cylindrical puck. However, increasing the diameter of the puck could result in the same trapped field at a lower J_c. Specifically, by doubling the diameter from 20 mm to 40 mm, the critical current density required to achieve a peak trapped field of 3 T was calculated to be 58.7 kA/cm^2 using the MoM analysis. Such a TFM would require a critical current density of about 62% that of its 2 cm diameter counterpart in order to achieve a trapped field of 3 T.

3. THERMAL ANALYSIS

As discussed in the previous chapters, it is necessary to keep the YBCO below its critical temperature in order for it to be in the mixed state. In the previous chapter, the TFM analysis and the results that were referenced were achieved by maintaining the temperature of the YBCO around liquid nitrogen temperatures of 77 K. Therefore, in order to ensure that the YBCO performs as shown in Section 2.3, its temperature must be held to at most 77 K. As a result, a thermal analysis of the machine must be included as part of the design process to monitor the temperature of the YBCO as well as other areas of the machine to ensure that overheating does not occur.

The use of Thermal Equivalent Circuits (TECs) to perform thermal analysis is discussed in Chapter 10 of [32]. Herein the equations of heat flow in a material that are used to develop a thermal model in [32] are reviewed. Then, the TEC elements developed therein are used to construct a thermal model of the machine whose cross-section was shown in Figure 2.1.

3.1 Heat Flow in a Material

The heat flow in a material is given by Fourier's law:

$$\mathbf{Q}'' = -\left(k_x \frac{\partial T}{\partial x}\mathbf{a_x} + k_y \frac{\partial T}{\partial y}\mathbf{a_y} + k_z \frac{\partial T}{\partial z}\mathbf{a_z}\right) \tag{3.1}$$

where $\mathbf{Q}''$ is the heat flux or the heat transfer rate per unit area (W/m^2), k is the thermal conductivity of the material (W/m·K), and ∇T is the temperature gradient (K/m). Then the heat transfer rate in Watts through a surface Γ is

$$\dot{Q}_\Gamma = \int_{S_\Gamma} \mathbf{Q}'' \cdot d\mathbf{S}. \tag{3.2}$$

This heat transfer rate is used to describe the rate of change of energy within the material. The energy density (J/m^3) of a material is given by $e = c\rho T$, where c is its specific heat capacity (J/kg·K), ρ is the density (kg/m^3), and T is the temperature in K. This quantity

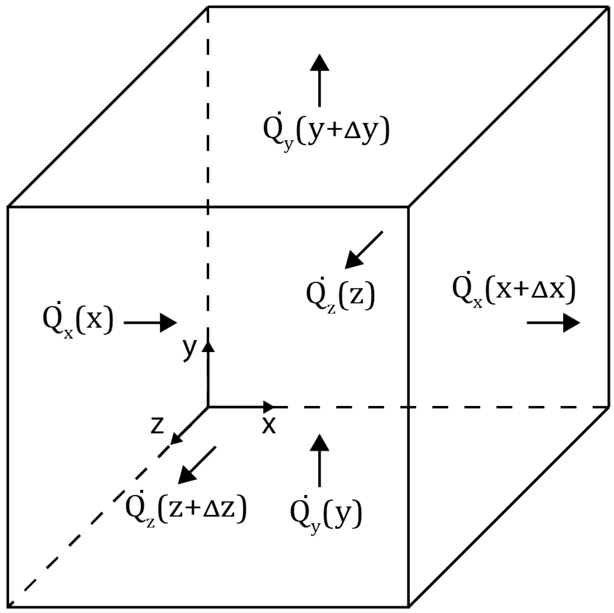

Figure 3.1. Cuboid element used in thermal energy calculations

is integrated over the volume of the material V_Ω to obtain the total thermal energy E_Ω. Integrating the entire equation for the energy density yields

$$E_\Omega = C_\Omega \langle T_\Omega \rangle \tag{3.3}$$

where $\langle T_\Omega \rangle$ is the spatially averaged temperature over the entire region defined by

$$\langle T_\Omega \rangle = \frac{1}{V_\Omega} \int_{V_\Omega} T_\Omega dV \tag{3.4}$$

and C_Ω is the thermal capacitance of the material in J/K.

The rate of change of thermal energy in a cube with dimensions $\Delta x \times \Delta y \times \Delta z$ shown in Figure 3.1 can be expressed as the sum of the power dissipated within the cube and the heat transfer rates through its six sides:

$$\frac{dE}{dt} = P + \dot{Q}_x(x) - \dot{Q}_x(x + \Delta x) + \dot{Q}_y(y) - \dot{Q}_y(y + \Delta y) + \dot{Q}_z(z) - \dot{Q}_z(z + \Delta z) \tag{3.5}$$

For a sufficiently small cube, the thermal energy density and the power dissipation density can be assumed constant throughout the volume, in which case the previous equation is rewritten as

$$\begin{aligned}\Delta x \Delta y \Delta z \frac{de}{dt} =& \Delta x \Delta y \Delta z p \\ &+ \dot{Q}_x(x) - \dot{Q}_x(x+\Delta x) \\ &+ \dot{Q}_y(y) - \dot{Q}_y(y+\Delta y) \\ &+ \dot{Q}_z(z) - \dot{Q}_z(z+\Delta z)\end{aligned} \tag{3.6}$$

Using (3.1) and (3.2), the heat transfer rates can be rewritten as the integral of the temperature gradient across the respective sides of the cube. For the heat transfer rate in the x direction, this is

$$\dot{Q}_x(x) - \dot{Q}_x(x+\Delta x) = k_x \int_{S_x} \frac{\partial T(x+\Delta x, y, z)}{\partial x} - \frac{\partial T(x,y,z)}{\partial x} dS \tag{3.7}$$

Again assuming small Δx, Δy, and Δz,

$$\dot{Q}_x(x) - \dot{Q}_x(x+\Delta x) = k_x \int_{S_x} \Delta x \frac{\partial^2 T(x,y,z)}{\partial x^2} dS = k_x \Delta x \Delta y \Delta z \frac{\partial^2 T(x,y,z)}{\partial x^2} \tag{3.8}$$

Repeating for the heat transfer rates in the remaining two directions,(3.6) is rewritten as

$$\frac{de}{dt} = p + k_x \frac{\partial^2 T}{\partial x^2} + k_y \frac{\partial^2 T}{\partial y^2} + k_z \frac{\partial^2 T}{\partial z^2} \tag{3.9}$$

3.2 Developing TEC Elements

Equation (3.9) was then used used to develop thermal equivalent circuits for regions of several different shapes in [32]. For a cuboidal region with dimensions $0 \leq x \leq l_{\Omega_x}$, $0 \leq y \leq l_{\Omega_y}$, and $0 \leq z \leq l_{\Omega_z}$, the temperature is assumed to satisfy

$$T_\Omega = c_{2x}x^2 + c_{1x}x + c_{2y}y^2 + c_{1y}y + c_{2z}z^2 + c_{1z}z + c_0 \tag{3.10}$$

and the flow of heat is independent in all 3 directions. Taking the spatial average of this temperature distribution across the entire region yields

$$\langle T_\Omega \rangle = \frac{1}{3}c_{2x}l_{\Omega x}^2 + \frac{1}{2}c_{1x}l_{\Omega x} + \frac{1}{3}c_{2y}l_{\Omega y}^2 + \frac{1}{2}c_{1y}l_{\Omega y} + \frac{1}{3}c_{2z}l_{\Omega z}^2 + \frac{1}{2}c_{1z}l_{\Omega z} + c_0 \tag{3.11}$$

Taking the spatial average of the temperature at its sides $x = 0$ and $x = l_{\Omega x}$ and comparing to (3.10) yields the following:

$$\langle T_{\Omega 0x} \rangle = \langle T_\Omega \rangle - \frac{1}{3}c_{2x}l_{\Omega x}^2 - \frac{1}{2}c_{1x}l_{\Omega x} \tag{3.12}$$

$$\langle T_{\Omega lx} \rangle = \langle T_\Omega \rangle + \frac{2}{3}c_{2x}l_{\Omega x}^2 + \frac{1}{2}c_{1x}l_{\Omega x} \tag{3.13}$$

Differentiating the assumed temperature distribution with respect to x yields

$$\frac{\partial T_\Omega}{\partial x} = 2c_{2x}x + c_{1x} \tag{3.14}$$

and then using (3.1) and (3.2) at $x = 0$ and $x = l_{\Omega x}$, respectively, expressions for the heat transfer rates in the x direction at the two faces, $\dot{Q}_{\Omega 0x}$ and $\dot{Q}_{\Omega lx}$, can be found. These are then used to solve for the two coefficients c_{2x} and c_{1x}. Finally, the following equations are obtained:

$$\langle T_{\Omega 0x} \rangle = T_{\Omega cx} + R_{\Omega x}\dot{Q}_{\Omega 0x} \tag{3.15}$$

$$\langle T_{\Omega lx} \rangle = T_{\Omega cx} - R_{\Omega x}\dot{Q}_{\Omega lx} \tag{3.16}$$

$$T_{\Omega cx} = \langle T_\Omega \rangle - \frac{1}{3}R_{\Omega x}(\dot{Q}_{\Omega 0x} - \dot{Q}_{\Omega lx}) \tag{3.17}$$

where $R_{\Omega x}$ is the thermal resistance of the material in the x-direction, defined as

$$R_{\Omega x} = \frac{l_{\Omega x}}{2k_{\Omega x}S_{\Omega x}} \tag{3.18}$$

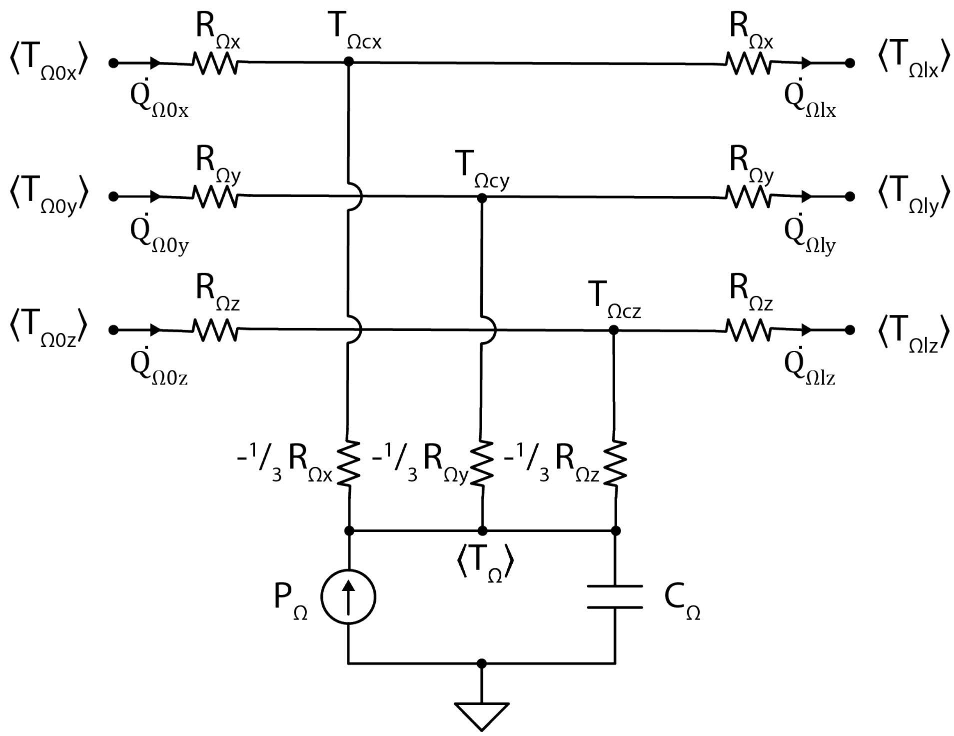

Figure 3.2. TEC of Cuboidal Region

and where $S_{\Omega x}$ is the surface area of the $x = 0$ or $x = l_{\Omega x}$ face of the cuboidal region. Repeating for the remaining directions yields identical equations for the average temperature of each face. Assembling together, the steady state temperature distribution is be found in the element. The transient behavior can be incorporated after taking the spatial average of the energy density in (3.9) and multiplying by the volume, which yields the following result:

$$\frac{d\langle T_\Omega \rangle}{dt} = \frac{1}{C_\Omega}(P_\Omega + \dot{Q}_{\Omega 0x} - \dot{Q}_{\Omega lx} + \dot{Q}_{\Omega 0y} - \dot{Q}_{\Omega ly} + \dot{Q}_{\Omega 0z} - \dot{Q}_{\Omega lz}) \tag{3.19}$$

Using (3.15) - (3.18) along with the corresponding equations for the heat flow in the y and z directions and (3.19), the cuboidal TEC element shown in Figure 3.2 was formed in [32]. As can be seen in this figure, the heat flow in the element is modeled using analogous electrical circuit elements, where the resistances represent the thermal resistance of the element in each direction, and the capacitor represents the thermal capacitance and transient behavior of the element. Using this model, the heat flow and temperatures can be found in the element using electrical circuit analysis techniques. It is worth noting that while the temperatures at the outer nodes correspond to the mean temperatures of each face of the element, the three central nodes are artificial nodes, and therefore the node temperatures $T_{\Omega cx}$, $T_{\Omega cy}$, and $T_{\Omega cz}$ are not real temperatures within the element.

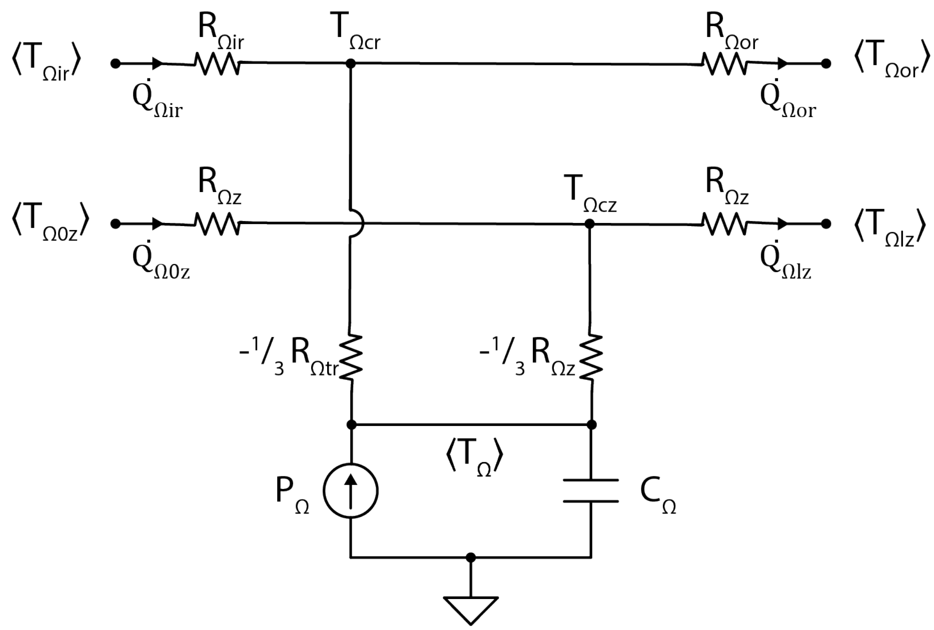

Figure 3.3. TEC of Cylindrical Region

A TEC model for a cylindrical region was also derived using a similar derivation as the cuboidal TEC above and is shown in Figure 3.3. This element represents a hollow cylinder extending from an inner radius r_i to an outer radius r_o over the angle θ, with an axial length l_z. In this element, the heat is assumed to flow in either the radial or axial directions. The equations for the axial heat flow and thermal resistance are the same as in the cuboidal element. The heat flow in the radial direction is given by the following equations:

$$\langle T_{\Omega ir} \rangle = T_{\Omega cr} + R_{\Omega ir}\dot{Q}_{\Omega ir} \tag{3.20}$$

$$\langle T_{\Omega or} \rangle = \langle T_{\Omega} \rangle + R_{\Omega tr}(\dot{Q}_{\Omega ir} - \dot{Q}_{\Omega or}) - R_{\Omega or}\dot{Q}_{\Omega or} \tag{3.21}$$

$$T_{\Omega cr} = \langle T_{\Omega} \rangle + R_{\Omega tr}(\dot{Q}_{\Omega ir} - \dot{Q}_{\Omega or}) \tag{3.22}$$

where the thermal resistances are defined using

$$R_{\Omega ir} = \frac{1}{2k_{\Omega r}\theta_{\Omega r}l_{\Omega z}}\left(\frac{2r_{\Omega o}^2}{r_{\Omega i}^2 - r_{\Omega o}^2}\ln\left(\frac{r_{\Omega o}}{r_{\Omega i}}\right) - 1\right) \tag{3.23}$$

$$R_{\Omega or} = \frac{1}{2k_{\Omega r}\theta_{\Omega r}l_{\Omega z}}\left(1 - \frac{2r_{\Omega i}^2}{r_{\Omega i}^2 - r_{\Omega o}^2}\ln\left(\frac{r_{\Omega o}}{r_{\Omega i}}\right)\right) \tag{3.24}$$

$$R_{\Omega tr} = -\frac{1}{4k_{\Omega r}\theta_{\Omega r}(r_{\Omega o}^2 - r_{\Omega i}^2)l_{\Omega z}}\left(r_{\Omega i}^2 + r_{\Omega o}^2 - \frac{4r_{\Omega i}^2 r_{\Omega o}^2}{r_{\Omega o}^2 - r_{\Omega i}^2}\ln\left(\frac{r_{\Omega o}}{r_{\Omega i}}\right)\right) \tag{3.25}$$

As with the cuboidal element, this TEC element can be used to solve the node temperatures and heat flow in the element. As before, $T_{\Omega cr}$ and $T_{\Omega cz}$ are the temperatures at the artificial central nodes and do not correspond to real temperatures within the element.

3.3 TEC of YBCO Machine

Using the two TEC elements that were discussed in the previous section, a thermal model was developed for the YBCO-based machine introduced in Chapter 2. Using cylindrical and cuboidal TEC elements a thermal equivalent circuit model was developed for a section of the machine using the Thermal Equivalent Toolbox [52] as shown in Figure 3.4. Due to the radial symmetry, the flow of heat is also assumed to have symmetry, so only a small sector of the cross section of the machine was represented in the thermal model. The TEC spans a section of the machine with an angle of π/S_s, or half of one stator tooth and half of one slot, and extends to the length of the machine in the axial direction.

The TEC that was formed for this machine is shown in Figure 3.5. Beginning at the center of the machine is the rotor shaft, which is represented by the cylindrical element A. It has an inner radius of 0 and outer radius r_{rs}. The rotor and stator elements extend to the active length of the machine l in the axial direction. The shaft extends past the other rotor elements in both directions. The rotor inert region is represented by the cylindrical element B. It extends from r_{rs} to r_{ri} with an axial length of l. Cylindrical element C is the rotor backiron segment extending from r_{ri} to r_{cp} over the angle π/S_s. The cryogenic cooling plate

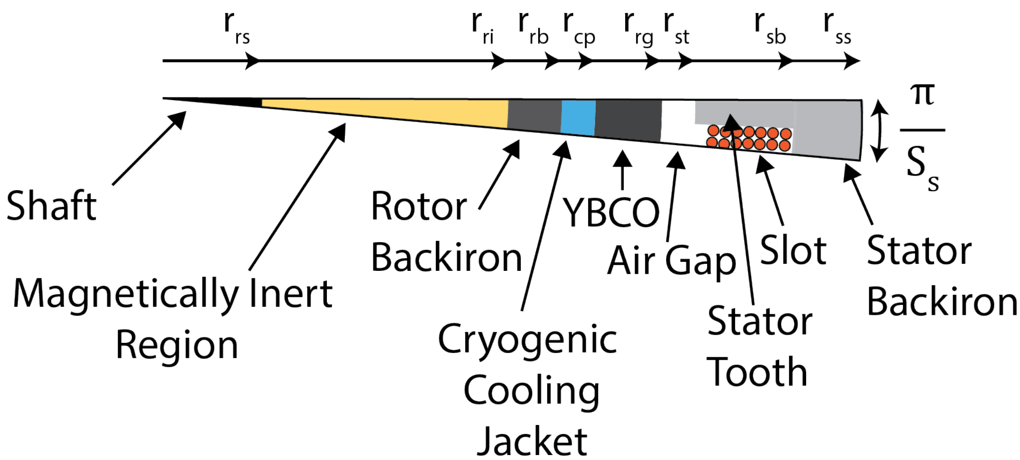

Figure 3.4. Section of YBCO Machine used in TEC

is assumed to have a constant temperature, so in the TEC it is represented as a temperature source with temperature T_{cp} in contact with the two neighboring elements.

The YBCO material is element D in the TEC in Figure 3.5. Since the YBCO used in similar applications is typically in the form of pucks with rectangular cross sections ([6], [5], [9],[10],[51]), it was modeled using a cuboidal element. Continuing outward in the machine toward the air gap is the stator. The stator as shown in 3.4 is represented by 4 cuboidal elements E-H. Element E represents half of a stator tooth and element F represents the conductors in half of a stator slot. With the x-axis being in the radial direction and the z-axis out of the page, these two regions have lengths in the x direction equal to the depth of the tooth and the winding depth, respectively. Their length in the y direction is equal to half of the tooth or slot width, respectively, and both extend to the active length of the machine l in the z direction. Elements G and H are the stator backiron segments adjacent to the tooth and slot winding elements, respectively. Their lengths in the x direction are equal to the depth of the backiron and have the same y and z dimensions as elements D and E.

The conductors in the slot windings extend axially and wrap around the stator teeth to form end windings. Since the end windings extend axially on both sides of the machine, elements I and J represent the end winding on the front of the machine and elements K and L represent the end winding on the back of the machine. Elements J and L represent the

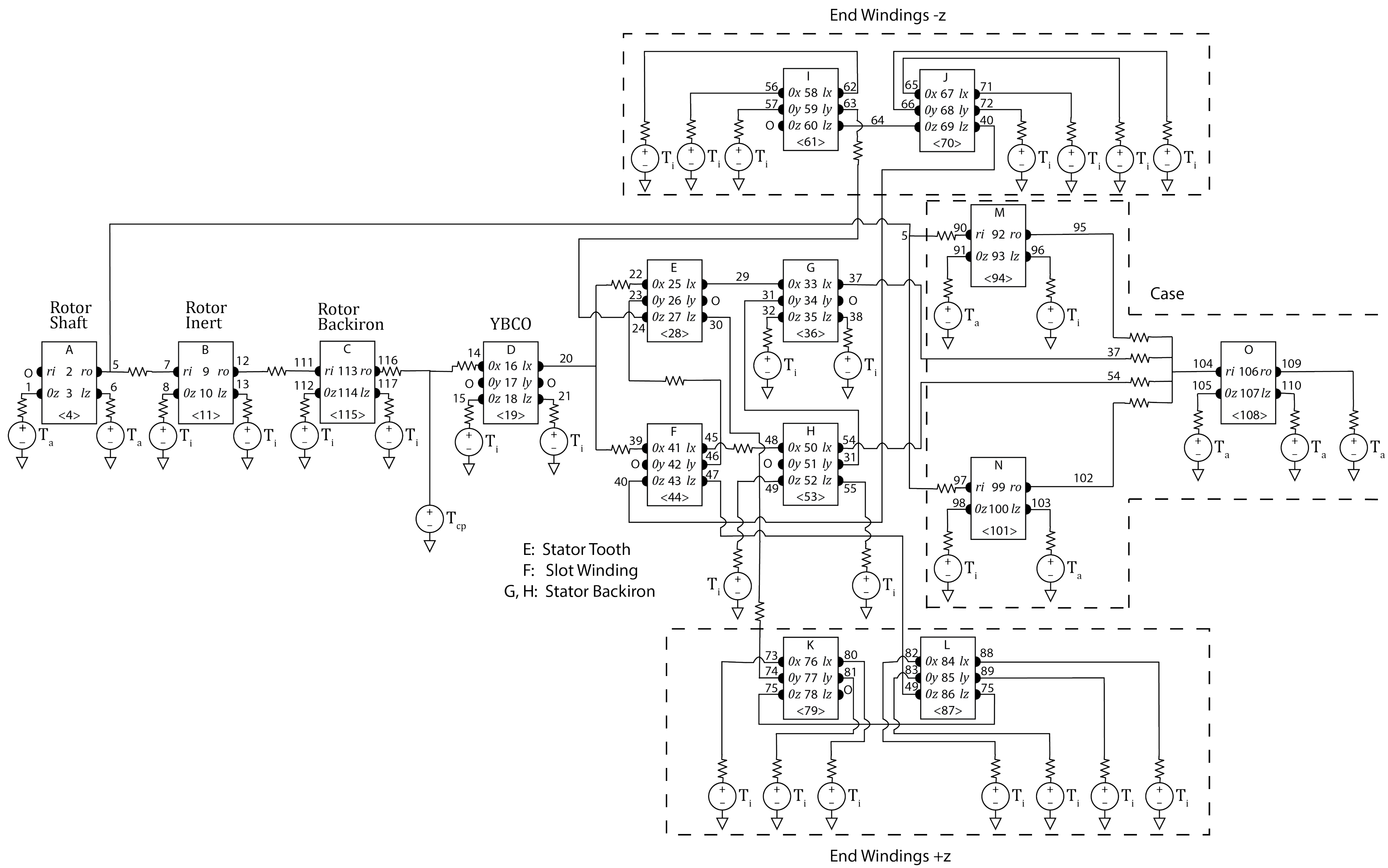

Figure 3.5. Thermal Equivalent Circuit of YBCO Machine

conductors extending from the slot above element F, and elements I and K represent the part of the end winding above the tooth.

The machine was modeled as enclosed within a cylindrical case represented by cylindrical elements M-O. These are not shown in Figure 3.4. Cylindrical elements M and N are the two end caps of the case and they extend from an inner radius r_{rs} to outer radius r_{ss} above and below the machine. Element O is the outer shell of the case connected to elements M and N, and is also in contact with the stator backiron elements G and H.

Each of the elements described here is either a cuboidal or cylindrical element shown in Figures 3.2 and 3.3, and the thermal resistances in each of the branches shown in these two elements can be calculated using the thermal conductivity k and the dimensions of the region represented by the TEC element. In Figure 3.5 only the outer nodes corresponding to the average temperature at each of the element's faces are shown, and the node numbers shown in the center correspond to the center nodes and the node corresponding to the mean temperature within the element, respectively.

Since the regions corresponding to the slot and end windings are composed of several materials with different thermal conductivities, the winding regions are represented as homogeneous regions within the TEC. These calculations were performed in Chapter 10 of [32]. The winding region used for these calculations is shown in Figure 3.6. The conductor material is denoted by the subscript c, and the layer of insulation around each conductor by the subscript i. The air surrounding the conductors is denoted by the subscript a. To find the thermal conductivities in the homogenized region, the three materials are first lumped together by area as shown in Figure 3.6, where the aspect ratio of each region is the same as the original winding area $\zeta = \frac{w}{d}$. The thermal conductivities are obtained by calculating the thermal resistance of this new region assuming a combination of parallel connections of series thermal resistances (from left to right in Figure 3.6) and comparing to the equation for thermal resistance in one dimension:

$$R_x = \frac{l_x}{k_x S_x} \tag{3.26}$$

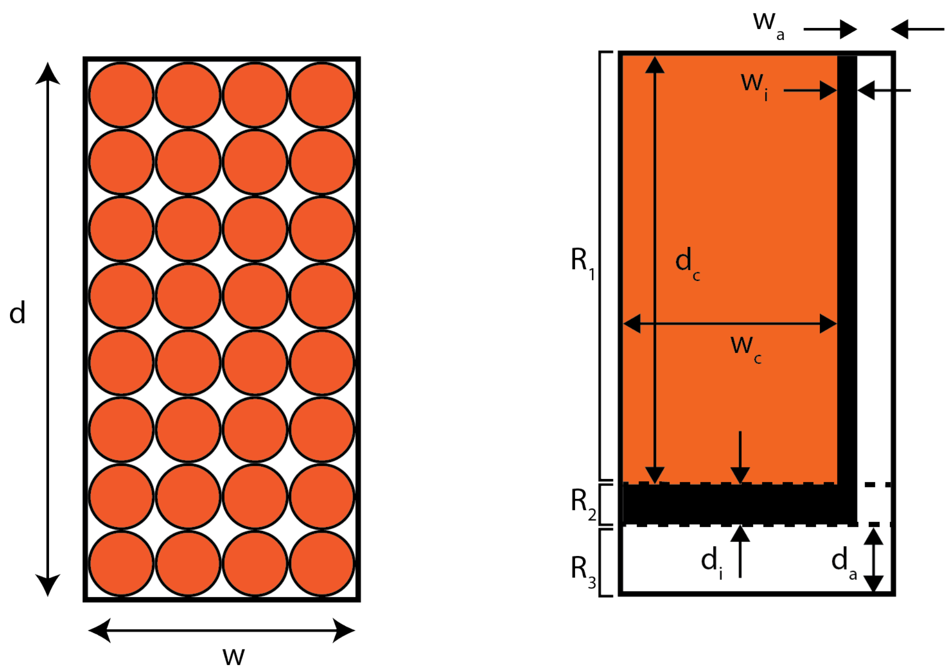

Figure 3.6. Geometry for Homogenized Winding Region Calculation

The thermal conductivities in the homogenized region are determined to be

$$k_{xye} = \frac{1}{\dfrac{1}{k_c} + \dfrac{w_i}{k_i w_c} + \dfrac{w_a}{k_a w_c}} + \frac{1}{\dfrac{w_c + w_i}{k_i w_i} + \dfrac{w_a}{k_a w_i}} + \frac{1}{\dfrac{w}{k_a w_a}} \tag{3.27}$$

and

$$k_{ze} = \frac{a_c}{wd} k_c + \frac{a_i}{wd} k_i + \frac{a_a}{wd} k_a \tag{3.28}$$

where k_c, k_i, and k_a are the thermal conductivities of the conductor, insulation, and air, respectively. The thermal conductivity k_{xye} is the conductivity in the x and y directions for the flow of heat through the winding cross section, and k_{ze} is the thermal conductivity of the winding bundle in the z direction, moving in the same direction as the conductors.

The thermal equivalent circuit shown in Figure 3.5 also shows other thermal resistances and temperature sources not pertaining to the thermal resistances within each element. These result from either a contact resistance between two elements or a resistance associated with the transfer of heat from a solid object to a fluid. The contact resistance occurs due to surface irregularities between objects and therefore the two objects are not in perfect contact. This thermal resistance is given by

$$R_{ct} = \frac{1}{A_{ct} h_{ct}} \tag{3.29}$$

where A_{ct} is the contact area and h_{ct} is a heat transfer coefficient for the contact between the two objects. The other type of resistance shown in this TEC is due to convective heat transfer from a solid to a moving fluid, such as the heat transfer from the case to the surrounding air. This resistance is given by

$$R_{cv} = \frac{1}{A_{cv} h_{cv}} \tag{3.30}$$

where A_{cv} is the again contact area and h_{cv} is a convective heat transfer coefficient.

In the TEC shown in Figure 3.5, the exterior of the case is connected to the ambient air temperature outside the machine T_a, which was assumed to be 300 K. All of the nodes corresponding to surfaces inside the machine that are in contact with air were connected to a temperature source corresponding to the interior air temperature T_i. Since the air temperature in the end cap regions is unknown, it was represented as an additional node temperature to be solved along with the rest of the node temperatures.

The thermal conductivities used to calculate the thermal resistances within each TEC element are properties of the material and can be readily found. The thermal conductivity of the different materials in the YBCO machine are given in Table 3.1. However, the heat transfer coefficients for contact resistances and convective heat transfer depend on the materials as well as surface irregularities and how well the materials are in contact, and is therefore a much more complicated problem.

In [55], Mellor et al. give values for the heat transfer coefficient for the stator core to frame contact with respect to the contact pressure. In the thermal model of the YBCO machine, this coefficient, h_{cc}, was chosen to be 500 W/m^2K, corresponding to a contact pressure of 1 MPa. This value was used to calculate the contact resistance between the stator backiron and the case, as well as any other metal-metal contact resistances within the machine, such

Table 3.1. Thermal Conductivity of Materials in YBCO Machine

Material	Thermal Conductivity (W/(m·K))
Steel (Hiperco 50)	$k_s = 29.8$
Copper	$k_{cu} = 385$
Aluminum	$k_{al} = 205$
YBCO [53]	$k_{ybco,x} = 2.5$ $k_{ybco,y} = 15$ $k_{ybco,z} = 15$
Wire Insulation	$k_{ins} = 0.4$
Inert [54]	$k_{mi} = 0.7$
Air (300 K)	$k_a = 0.0263$

as the rotor backiron and the copper cooling plate. In [56] the contact resistance between steel and polycarbonate materials was studied, and based on their data, in this TEC a value of 250 W/m^2K was used for the core-inert contact heat transfer coefficient h_{ci}. In [32] the contact resistance between the stator iron and the winding was calculated, and the heat transfer coefficient was determined to be

$$h_{cw} = \frac{4h_{sl}k_a}{4k_a + (4-\pi)h_{sl}r_c} \tag{3.31}$$

where k_a is the thermal conductivity of air and r_c is the radius of the conductors. This calculation assumes a slot liner with a heat transfer coefficient of $h_{sl} = 560$ W/m^2K and that there is no gap between the winding and the core. These values are summarized in Table 3.2.

Table 3.2. Heat Transfer Coefficients for Contact Resistances

Heat Transfer Coefficient (W/m^2K)
$h_{cc} = 500$
$h_{ci} = 250$
$h_{sl} = 560$
$h_{cw} = \frac{4h_{sl}k_a}{4k_a + (4-\pi)h_{sl}r_c}$

In [55] the value of the convective heat transfer coefficient for the end cap air is given by $h_{ca} = 15.5(0.29v + 1)$ W/m^2K where v is the air velocity inside the machine and h_{ca} was assumed to be linear for air velocities below 7.5 m/s. Mellor et al. estimated the air velocity due to a cooling fan as $v = r_m \omega_r \eta$ where r_m is the radius of the fan, ω_r is the angular velocity of the rotor, and η is the efficiency, which was assumed to be 50%. In [55] the convective heat transfer coefficient of the end windings was assumed to be 50% higher due to the larger surface area, and therefore $h_{wa} = 1.5h_{ca}$. The heat transfer coefficient h_{ca} was also used to calculate the thermal resistance from the exterior of the case to ambient, using an air velocity of 0, representing natural convection.

A heat transfer coefficient used to calculate the air gap thermal resistance is given in [57]. The authors of this paper calculate the air gap thermal resistance using the modified Taylor number

$$T_{am} = \frac{T_a}{F_g} \tag{3.32}$$

where

$$T_a = \frac{\omega_r^2 R_m g^3}{\nu^2} \tag{3.33}$$

$$F_g = \frac{\pi^4}{P} \frac{1}{1697(1 - g/2R_m)^2} \tag{3.34}$$

$$P = 0.0571(1 - 0.625x) + \frac{0.00056}{1 - 0.625x} \tag{3.35}$$

$$x = \frac{g/R_m}{1 - g/2R_m} \tag{3.36}$$

where ω_r is the rotational speed of the rotor, g is the width of the air gap, R_m is the mean air gap radius, and ν is the kinematic viscosity, which for air at 300 K is 1.569e-6 m^2/s. This is then used to calculate the nusselt number given by:

$$Nu = \begin{cases} 2 & 0 \leq T_{am} \leq 1700 \\ 0.128 T_{am}^{0.367} & 1700 \leq T_{am} \leq 10^4 \\ 0.409 T_{am}^{0.241} & 10^4 \leq T_{am} \leq 10^7 \end{cases} \tag{3.37}$$

Finally, the heat transfer coefficient is given by

$$h_{gap} = \frac{k_a Nu}{2g} \tag{3.38}$$

where k_a is the thermal conductivity of air. The heat transfer coefficients used for calculating convective heat transfer are given in Table 3.3.

Table 3.3. Convective Heat Transfer Coefficients

Heat Transfer Coefficient (W/m^2K)
$h_{ca} = 15.5(0.29v + 1)$, $v \leq 7.5$ m/s
$h_{wa} = 1.5h_{ca}$
$h_{gap} = \frac{k_a Nu}{2g}$

Based upon the thermal conductivities and heat transfer coefficients for the different materials, the TEC of the YBCO machine was formed and solved using the Thermal Equivalent Circuit Toolbox 2.0 [52]. Using this toolbox, the TEC shown in Figure 3.5 was constructed using cylindrical and cuboidal elements and by placing additional branches for the contact resistances between elements and convective heat transfer to the surrounding air.

The magnetic core loss and resistive losses within the machine are determined in the electromagnetic analysis. The calculation of these quantities will be discussed in the next chapter. These losses are then added within the stator steel and winding elements, respectively, according to the volume of the element with respect to the entire volume of the region in the machine. These losses act to increase the temperature within the stator steel and winding elements. The resistivity of the conductors is temperature dependent, and therefore as the temperature in the winding increases, so will the resistive losses. In Chapter 10 of [32], the conductivity of the conductors in element Ω is given by

$$\sigma_{\Omega} = \frac{\sigma_{0c}}{1 + \alpha_c(\langle T_{\Omega} \rangle - T_{0c})} \tag{3.39}$$

where σ_{0c} is the nominal conductivity at a nominal temperature T_{0c} and α_c is a coefficient related to the temperature of the conductor. Using this conductivity, the loss within the element is recalculated as

$$P_\Omega = \frac{V_{c\Omega} J^2}{\sigma_\Omega} \tag{3.40}$$

To solve for the temperatures within a machine, an initial TEC is formed with no power dissipation in the winding regions. An initial vector $\mathbf{T}$ of the temperatures at all of the nodes is initialized to the ambient temperature T_a. The resistive loss for each of the winding elements is calculated with a mean temperature of T_a. These losses are then added to their respective elements and the TEC is solved and the mean temperature within each winding element is calculated. The mean temperature within each of the winding elements is then used to calculate new conductivities and update the loss in each of the elements. This process is repeated and the temperatures are iteratively solved until the error, defined as $e = max(|\mathbf{T} - \mathbf{T}_{old}|)$, is below a threshold of 5 mK or a maximum of 50 iterations was reached.

As part of the thermal analysis the temperature source T_{cj} is also lowered until the peak temperature in the YBCO element is below a maximum specified value. The final temperature distribution is achieved when both the error criterion is met and the peak temperature in the YBCO is below its maximum value. In the multi-objective optimization that is described in Chapter 4, the performance of each candidate machine is evaluated based on it's total mass and loss. Therefore, for the YBCO machine, the mass and power required by a cryocooler to cool the YBCO to the specified temperature must also be included. A model of the cryocooler is provided in the next chapter. Here is noted that its size is a function of the amount of power that must be extracted. The power extracted was calculated as the total amount of power flowing from the YBCO to the cooling plate, as well as power from the rotor backiron and the endcap air on both ends of the machine. The power flowing from the YBCO to the cooling plate was calculated as

$$P_{ext,D} = (T_{D0x} - T_{cp}) S_{Dx} h_{cc} \tag{3.41}$$

where the subscript D indicates element D representing the YBCO and S_{Dx} is the contact area and h_{cc} is the heat transfer coefficient. Similar calculations are performed for the flow of heat from the rotor backiron and endcap air to the cooling plate. Since only a fraction of the machine corresponding to an angle of π/S_s, the sum of these 4 quantities is then multiplied by $2S_s$ to obtain the total amount of power that must be extracted from the machine by the cryocooler.

4. DESIGN STUDY

In the previous chapters, models for the electromagnetic and thermal performance of the YBCO machine were provided. In this chapter, these models are used to evaluate the performance of the machine using a series of multi-objective design studies. For the studies, a genetic algorithm (GA) is used to find an optimal set of designs subject to a set of specifications. The performance objectives include the minimization of both the mass and power loss in the machine and inverter. The machine parameters are represented as genes within the GA, and the Genetic Optimization System Engineering Toolbox (GOSET) [58], was used to perform the optimization.

4.1 Design Parameters and Constraints

This section outlines the design structure, and the design specifications and machine parameters used for evaluating each design. The design study that is initially detailed here is for a 10 kW machine operating at 1800 rpm. The full list of specifications is given in Table 4.1. In the next section, the results of the YBCO machine design study are compared with a design for a standard PMSM. It is assumed that the PMSM adhered to the same specifications.

A list of the machine parameters used in this design study is shown in Table 4.2. These parameters are represented as genes within the GA and can take values within the shown intervals. The parameters are used to select the materials, geometry, and winding function, and many of these parameters are identical to those used in the design of a PMSM. Specifically, the geometry and winding function calculations detailed in [32].

These parameters are input into a fitness function in which the fitness of the design is evaluated and a number of constraints are imposed to ensure that all of the design specifications are met. Since a large number of design evaluations are performed within the GA, it is desired to minimize the time required for each fitness evaluation. Therefore, the number of constraints that have been satisfied is checked multiple times during fitness evaluation. This

Table 4.1. Design Specifications

Parameter	Value	Description
P_{out}^*	10 kW	required output power
ω_{rm}	1800 rpm	mechanical rotor speed
T_e^*	53.05 Nm	required torque
v_{dc}	625 V	dc voltage
r_{rs}	1 cm	shaft radius
k_{pf}	0.5	winding packing factor
l_{eo}	1 cm	end winding offset length
v_{fs}	2 V	semiconductor forward voltage drop
J	4	number of rotor positions to evaluate
m_{lim}	35 kg	mass limit
$P_{l,lim}$	1 kW	loss limit
ts_{mx}	190 m/s	maximum rotor tip speed
α_{tar}	10	maximum tooth aspect ratio
α_{so}	1.5	slot opening factor
n_{spp}	2	number of slots/pole/phase
k_m	0.75	demagnetization factor
$T_{mx,wdg}$	400 K	maximum winding temperature

allows the optimization to exit the fitness calculation without performing all of the required analysis if a prior constraint is found to be violated. The fitness is computed as [32]

$$\mathbf{f} = \begin{cases} \epsilon[1 \quad 1]^T \left(\dfrac{C_S - N_C}{N_C}\right) & C_S < C_I \\ \left[\dfrac{1}{m} \quad \dfrac{1}{P_l}\right]^T & C_S = N_C \end{cases} \tag{4.1}$$

where C_S is the total number of constraints satisfied, C_I is the number of constraints that have been evaluated, and N_C is the total number of constraints. The constraints are compared to the specification using either a greater than or equal function (gte) or less than or equal function (lte) [32]. These functions assign a value of 1 if the constraint is satisfied, and a value between 0 and 1 if the constraint has not been satisfied. A complete list of all the design constraints for this machine are shown in Table 4.3.

The first 5 constraints are calculated based on the machine geometry and windings, as well as the stator currents. The first constraint limits the aspect ratio of the tooth depth (d_{st}) to its width (w_{tb}). The next constraint, c_2 ensures that the conductor diameter d_c is

Table 4.2. Design Parameters

Gene	Parameter	Description	Enc.	Min	Max
1	s_t	Stator steel type	int	5	5
2	r_t	Rotor steel type	int	5	5
3	c_t	Conductor type	int	1	2
4	B_{trap}	TFM trapped field	lin	0.5 T	3 T
5	P_p	Pole pairs	int	4	8
6	d_{ri}	Depth of inert region	log	5 mm	10 cm
7	d_{rb}	Depth of rotor backiron	log	5 mm	3 cm
8	d_m	Depth of TFM	log	2 mm	13 mm
9	g	Air gap	lin	0.5 mm	5 cm
10	d_{tb}	Depth of tooth base	log	5 mm	10 cm
11	α_t	Tooth fraction	lin	0.15	0.9
12	d_{sb}	Depth of stator backiron	log	5 mm	3 cm
13	α_{tfm}	Magnet fraction	lin	0.15	0.95
14	l	Active length	log	5 cm	50 cm
15	N_{s1}^*	Peak fundamental conductor density (cond/rad)	log	10	1000
16	α_3^*	Coefficient of third harmonic conductor density	lin	0.1	0.7
17	i_{qs}^{r*}	Q-Axis current	log	5	250
18	i_{ds}^{r*}	D-Axis current	lin	-50	0
19	d_{cp}	Depth of cooling plate	lin	2 mm	15 mm
20	N_{pc}	Number of parallel conductors	int	1	5

Table 4.3. Design Constraints

Constraint	Description
$c_1 = \text{lte}(d_{st}/w_{tb}, \alpha_{tar})$	Stator tooth aspect ratio
$c_2 = \text{lte}(d_c \alpha_{so}, w_{so})$	Slot opening width
$c_3 = \text{lte}(I_s/a_c, J_{lim} \cdot 1.5)$	Current Density
$c_4 = \text{lte}(m, m_{lim})$	Mass limit
$c_5 = \text{lte}(ts, ts_{mx})$	Rotor maximum tip speed
$c_6 = \text{lte}(v_{pk,ll}, v_{dc} - 2v_{fs})$	Line-line voltage
$c_7 = \text{lte}(\lvert\lvert \mathbf{B}_{t1cnc} \rvert\rvert_{max}, B_{s,lim})$	Magnetic field in stator tooth
$c_8 = \text{lte}(\lvert\lvert \mathbf{B}_{b1cnc} \rvert\rvert_{max}, B_{s,lim})$	Magnetic field in stator backiron
$c_9 = \text{lte}(B_{rbtnc,mx}, B_{r,lim})$	Tangential Magnetic field in rotor backiron
$c_{10} = \text{lte}(B_{rbrnc,mx}, B_{r,lim})$	Radial Magnetic field in rotor backiron
$c_{11} = \text{gte}(B_{tfmnc,mx}, B_{trap} k_m)$	TFM trapped field
$c_{12} = \text{lte}(\lvert\lvert \mathbf{B}_{t1c} \rvert\rvert_{max}, B_{s,lim})$	Magnetic field in stator tooth
$c_{13} = \text{lte}(\lvert\lvert \mathbf{B}_{b1c} \rvert\rvert_{max}, B_{s,lim})$	Magnetic field in stator backiron
$c_{14} = \text{lte}(B_{rbt,mx}, B_{r,lim})$	Tangential Magnetic field in rotor backiron
$c_{15} = \text{lte}(B_{rbr,mx}, B_{r,lim})$	Radial Magnetic field in rotor backiron
$c_{16} = \text{gte}(B_{tfm,mx}, B_{trap} k_m)$	TFM trapped field
$c_{17} = \text{gte}(T_{ec}, T_e^*)$	Electromagnetic torque
$c_{18} = \text{lte}(T_{pk,wdg}, T_{mx,wdg})$	Winding Temperature
$c_{19} = \text{lte}(T_{pk,tbco}, T_{mx,ybco})$	YBCO temperature
$c_{20} = \text{lte}(P_l, P_{l,lim})$	Power loss limit

smaller than the width of the slot opening (w_{so}) to ensure that the conductors will fit in the slot. The current density is calculated as the rms phase current I_s divided by the conductor area, where

$$I_s = \sqrt{\frac{(I_{qs}^r)^2 + (I_{ds}^r)^2}{2}}. \tag{4.2}$$

The current density constraint was originally included as a thermal constraint to prevent overheating in the windings. However, since the TEC was developed for this machine, it is not strictly needed. However, this constraint was kept and the current density limit was increased by 50% to exclude designs with high current densities that would be unlikely to satisfy the thermal constraints. The total mass is computed as the sum of the volumes of the rotor inert, rotor steel, cooling plate, YBCO, stator steel, and stator windings multiplied by their respective densities, and is then constrained by c_4. The next constraint limits the rotor tip speed, and is used to ensure that the magnets would not experience forces that would lead to detachment from the rotor.

After the first 5 constraints are evaluated, the electrical parameters are calculated and an analysis of the machine without any stator currents applied is performed using the MoM analysis discussed in Chapter 2. Then constraints c_6-c_{11} are checked to ensure the design specifications are satisfied. The electrical parameters of the machine are used to calculate the line-line voltage as

$$V_{qs}^r = R_s I_{qs}^r + \omega_r (L_d I_{ds}^r + \lambda_m'^r) \tag{4.3}$$

$$V_{ds}^r = R_s I_{ds}^r - \omega_r L_q I_{qs}^r \tag{4.4}$$

$$v_{ll,pk} = \sqrt{3}\sqrt{(V_{qs}^r)^2 + (V_{ds}^r)^2} \tag{4.5}$$

where R_s is the nominal winding resistance given by

$$R_s = \frac{V_c}{\sigma_0 a_c^2} \tag{4.6}$$

where V_c is the conductor volume and a_c is the cross-sectional area of the conductor. This line-line voltage is then checked by c_6 to ensure that this voltage can be supplied by an inverter for the dc voltage given in Table 4.1. Observation sheets are placed in the machine during the MoM analysis and used to calculate the magnetic field at several locations of interest [37]. The MoM analysis is performed as the rotor is swept over a number of positions. The resulting flux density waveforms in the stator backiron and teeth are evaluated, and their peaks are constrained by $B_{s,lim}$ in c_7 and c_8. Observation sheets are also placed in the rotor backiron and the peak tangential and radial magnetic fields in the rotor backiron are also constrained using c_9 and c_{10}. The next constraint, c_{11}, is used in the design of PMSMs to ensure that the permanent magnet does not become demagnetized. In Chapter 1, it was stated that the YBCO will return to a normal state if the field exceeds the upper critical field H_{c2}. However, this occurs for very high fields of 20 T or higher at 77 K [59], [60], and therefore is unlikely to occur in the machine. This constraint was included, however, to ensure that the field within the TFM was not significantly lower than the desired trapped field. This is due to the fact that demagnetization could occur if an external field was applied in the direction opposite to magnetization and then removed. In this case the removal of said field would result in an electromotive force that would cause the surface currents in the TFM to reverse direction.

The MoM analysis is repeated with the stator windings energized, and constraints c_{12}-c_{16} are checked. The time-varying magnetic fields in the stator teeth and backiron produce magnetic core loss in the material. The core loss has two components resulting from eddy currents and magnetic hysteresis. These are discussed in detail in Chapter 6 of [32]. The flux density waveforms generated in the stator tooth and backiron are used to calculate the core loss. The eddy current loss density is given by

$$p_e = k_e f \int_0^T \left(\frac{dB}{dt}\right)^2 dt \tag{4.7}$$

and the hysteresis loss density is

$$p_h = k_h \left(\frac{f_{eq}}{f_b}\right)^{\alpha-1} \left(\frac{\Delta B}{2B_b}\right)^{\beta} \frac{f}{f_b} \tag{4.8}$$

In the hysteresis loss density calculation

$$f_{eq} = \frac{2}{\Delta B^2 \pi^2} \int_0^T \left(\frac{dB}{dt} \right)^2 dt \tag{4.9}$$

and $\Delta B = 2B_{pk}$, $f_b = 1$, $B_b = 1$, and k_e, k_h, α, and β are material parameters. The combined eddy current and hysteresis loss are computed in both the stator tooth and backiron regions to get the total power loss densities p_{ct} and p_{cb}. The total core loss is finally calculated as

$$P_c = p_{ct} v_{st} + p_{cb} v_{sb} \tag{4.10}$$

where v_{st} and v_{sb} are the volumes of the tooth and backiron, respectively. A corrected electromagnetic torque is computed to account for the core loss and is given by

$$T_{ec} = \begin{cases} T_e & w_{rm} = 0 \\ T_e - \dfrac{P_c}{w_{rm}} & w_{rm} \neq 0 \end{cases} \tag{4.11}$$

Constraint c_{17} then compares this value with the required torque. The thermal analysis of the machine is then performed and constraints c_{18} and c_{19} are checked. Constraint c_{18} ensures the peak temperature in the windings does not become too high to prevent overheating and damage to the wire insulation. Constraint c_{19} checks if the peak temperature of the YBCO is below a specified maximum temperature. This maximum temperature $T_{mx,ybco}$ is related to the specified trapped field B_{trap}. In [61], it was shown that the critical current density and therefore the trapped field is temperature dependent and can be approximated by

$$B_t(T_2) = B_t(T_1) \left(\frac{T_c - T_2}{T_c - T_1} \right)^2 \tag{4.12}$$

where T_c is the critical temperature. The value of B_t was chosen to be 1.1 T at an initial temperature of $T_1 = 77$ K based on the trapped field that can be achieved in commercially-available YBCO material [62]. Then, based on the desired trapped field B_{trap} that was a design parameter, the temperature to which the YBCO must be cooled is calculated using (4.12).

The thermal analysis returns an updated value of the resistive loss in the windings P_r. The semiconductor loss in the inverter is calculated as

$$P_s = \frac{6\sqrt{2}}{\pi} v_{fs} I_s \tag{4.13}$$

and then the total loss in the machine is then given by

$$P_l = P_r + P_s + P_c \tag{4.14}$$

and constraint c_{20} checks this value against the maximum power loss.

The thermal analysis of the machine also returns the total power that must be extracted by the cryocooler to achieve the desired temperature in the YBCO, and this is used to estimate the size of the required cryocooler system. The cryocooler model (discussions with Drummond Fudge, Continuous Solutions) is given by

$$m_{cryo} = 0.17041L + 7.8311 \quad (kg) \tag{4.15}$$

$$P_{cryo} = (0.024189L + 0.58784) \cdot 1000 \quad (W) \tag{4.16}$$

The cryocooler model was not included in the constraint checks, but m_{cryo} and P_{cryo} were added to a machine's mass and loss respectively, for the mass and loss that were used to evaluate a machine's performance. The cryocooler model was found to have a significant contribution to the total mass and loss of the system and therefore the constraints imposed would not be satisfied, but it was included in the fitness evaluation so that the GA would attempt to optimize the system as a whole.

A three phase bridge inverter is shown in Figure 4.1. This inverter is used to convert the dc source voltage into ac voltages that are applied to the three phases of the electric machine. For this application, it is desired to operate the inverter in order to achieve a desired electromagnetic torque T_e^* in the machine. Since the torque is proportional to the magnitude of the stator currents, it is therefore desired to operate the inverter as a current source and to control the three phase currents in the machine.

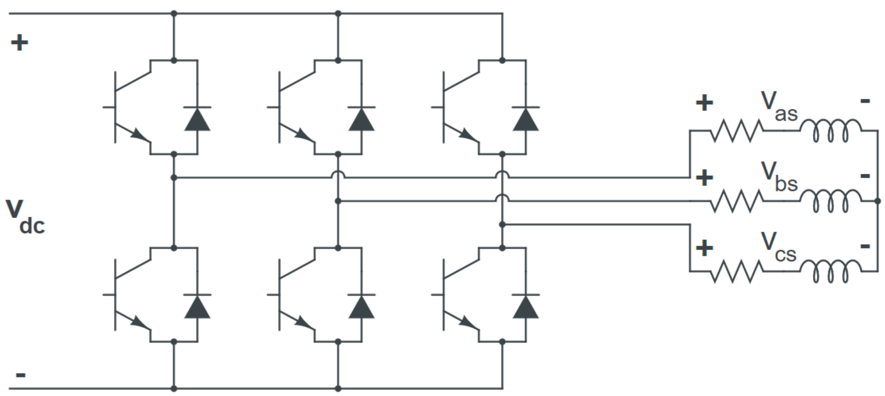

Figure 4.1. Three phase inverter

Therefore, it is desired to control the inverter to achieve the following balanced set of sinusoidal currents:

$$i_{as} = \sqrt{2}I_s cos(\theta_r + \phi_i) \tag{4.17}$$

$$i_{bs} = \sqrt{2}I_s cos(\theta_r + \phi_i - 2\pi/3) \tag{4.18}$$

$$i_{cs} = \sqrt{2}I_s cos(\theta_r + \phi_i + 2\pi/3) \tag{4.19}$$

where θ_r is the electrical rotor position ($\theta_r = \frac{P}{2}\theta_{rm}$) and ϕ_i is a phase offset. Transforming to qd variables in the rotor reference frame, these currents become

$$i_{qs}^r = \sqrt{2}I_s cos(\phi_i) \tag{4.20}$$

$$i_{ds}^r = -\sqrt{2}I_s sin(\phi_i) \tag{4.21}$$

In the GA, i_{qs}^{r*} and i_{ds}^{r*} are input parameters to machine analysis, where it is assumed that the inverter is able to provide the desired stator currents, so $i_{qs}^r = i_{qs}^{r*}$ and $i_{ds}^r = i_{ds}^{r*}$. The constraint c_6 as previously discussed, then ensures that the desired stator currents can be supplied by the source and that they do not cause line-line voltages in the machine greater than v_{dc} minus the voltage drop across the transistors and diodes in the inverter.

4.2 Design Results

In the previous section, the setup of the design parameters and constraints was discussed for a 10 kW YBCO machine design study. This optimization was performed using the GOSET toolbox [58] using a population size of 500 over 500 generations. Another optimization was performed for a PMSM with the same specifications and similar constraints to those shown in Table 4.3.

In order to ensure a fair comparison between the two optimizations, a TEC of the PMSM was also formed and the same peak winding temperature constraint was enforced in the PMSM. The TEC of the PMSM is the same as that of the YBCO machine shown in Figure 3.5, with a few exceptions. First, the YBCO element was replaced with a cylindrical TEC element representing the permanent magnet. Also, the temperature source representing the cryogenic cooling plate was removed and a thermal contact resistance was placed between the rotor backiron and permanent magnet.

The two optimizations were performed for both the PMSM and the YBCO machine. In each optimization, an optimal set of designs with minimum mass and loss were obtained. These two Pareto-optimal fronts are shown in Figure 4.2, and it shows the trade-off between mass and loss among both sets of optimal designs.

From Figure 4.2 it is clear that the PMSM has an advantage over the YBCO machine for this 10 kW, 1800 rpm optimization. To investigate the large separation between the two Pareto-optimal fronts, a machine from each was selected for comparison. The cross-section of the PMSM and the flux density waveforms in a stator tooth and backiron segment that were formed during the MoM analysis are shown in Figure 4.3 (a) and (b). The YBCO machine and its flux density waveforms are shown in (c) and (d). The TFMs in the YBCO machine had a trapped field of 3 T, which was the maximum value the GA could select. Due to the large trapped field, it can be seen that this YBCO machine has a much larger air gap

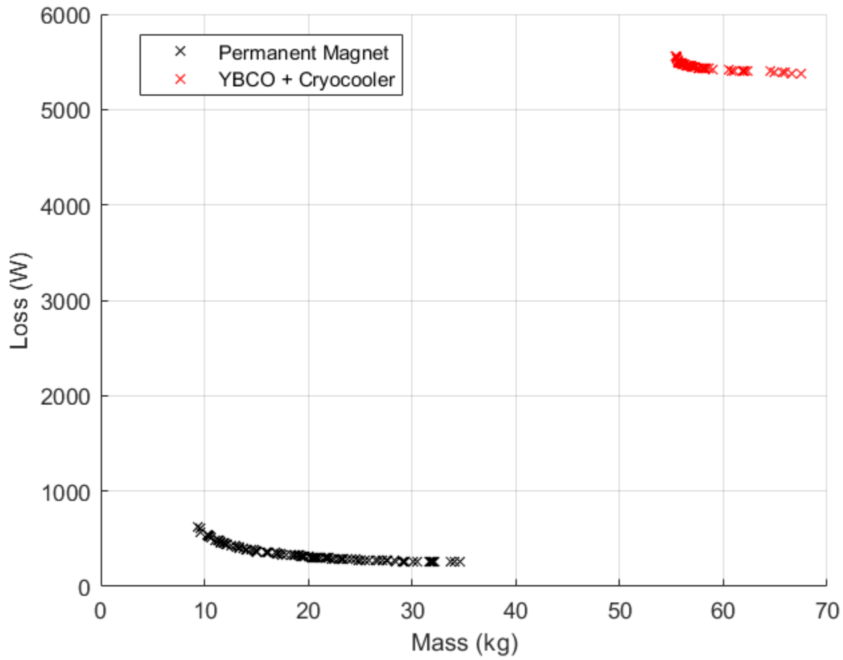

Figure 4.2. Pareto-Optimal Front (10 kW)

compared to the PMSM in Figure 4.3 in order to keep the flux density in the stator below the specified limit, which for Hiperco 50 is 2.07 T. A full list of the machine parameters selected by the GA for these two machines is given in Table 4.4.

A comparison of the performance of these two selected designs is shown in Table 4.5. It can be seen here that the primary reason for the large difference in the performance of the two machines is the additional mass and power of the cryocooler system. Although the YBCO machine and inverter for the selected design had an efficiency of 95.3%, which is comparable to the PMSM, the addition of the cryocooler system reduced the overall efficiency to 64.3%. In addition, the cryocooler accounts for 70.8% of the total mass of the system. On average, the YBCO machines on the Pareto-optimal front have a machine/inverter efficiency of 95.4%, but the efficiency with the cryocooler included is 64.7% on average. The average mass of the YBCO machine/cryocooler system is 57.7 kg with m_{cryo} contributing 67% of the total mass. The average efficiency of the PMSMs was 96.6%, with an average mass of 19.7 kg.

It is worth noting here that comparing designs from the two Pareto-optimal fronts strictly in terms of the machine and inverter performance may not be a fair comparison. This is

Table 4.4. Machine Parameter Comparison (10 kW)

Description	**Symbol**	**PMSM**	**YBCO Machine**
Stator steel type	s_t	Hiperco50 (μ_r = 42,892)	Hiperco50 (μ_r = 42,892)
Rotor steel type	r_t	Hiperco50 (μ_r = 42,892)	Hiperco50 (μ_r = 42,892)
Conductor type	c_t	Copper	Copper
Magnet type	m_t	NdFeB N35 (B_r = 1.19 T)	TFM (B_{trap} = 3 T)
Poles	P	14	8
Slots	S_s	84	48
Shaft Radius	r_{rs}	2 cm	2 cm
Depth of inert region	d_{ri}	5.83 cm	1.64 cm
Depth of rotor backiron	d_{rb}	0.91 cm	0.35 cm
Depth of cooling plate	d_{cp}	N/A	1.68 cm
Depth of magnet	d_m	1.19 cm	0.41 cm
Magnet fraction	α_m	73.5%	95%
Air gap	g	1.13 mm	16.1 mm
Depth of Tooth Base	d_{tb}	1.81 cm	3.44 cm
Tooth Fraction	α_t	48.2%	40.3%
Depth of stator backiron	d_{sb}	1.05 cm	0.67 cm
Active length	l	6.99 cm	6.47 cm
A-Phase Winding Pattern (1st Pole)	N_{as}	0 0 5 9 5 0	0 0 8 15 8 0
Conductor diameter	d_c	2.19 mm	3.2 mm
Q-Axis Current	I_{qs}^r	21.12 A	44.2 A
D-Axis Current	I_{ds}^r	-1.23 A	-4.33 A

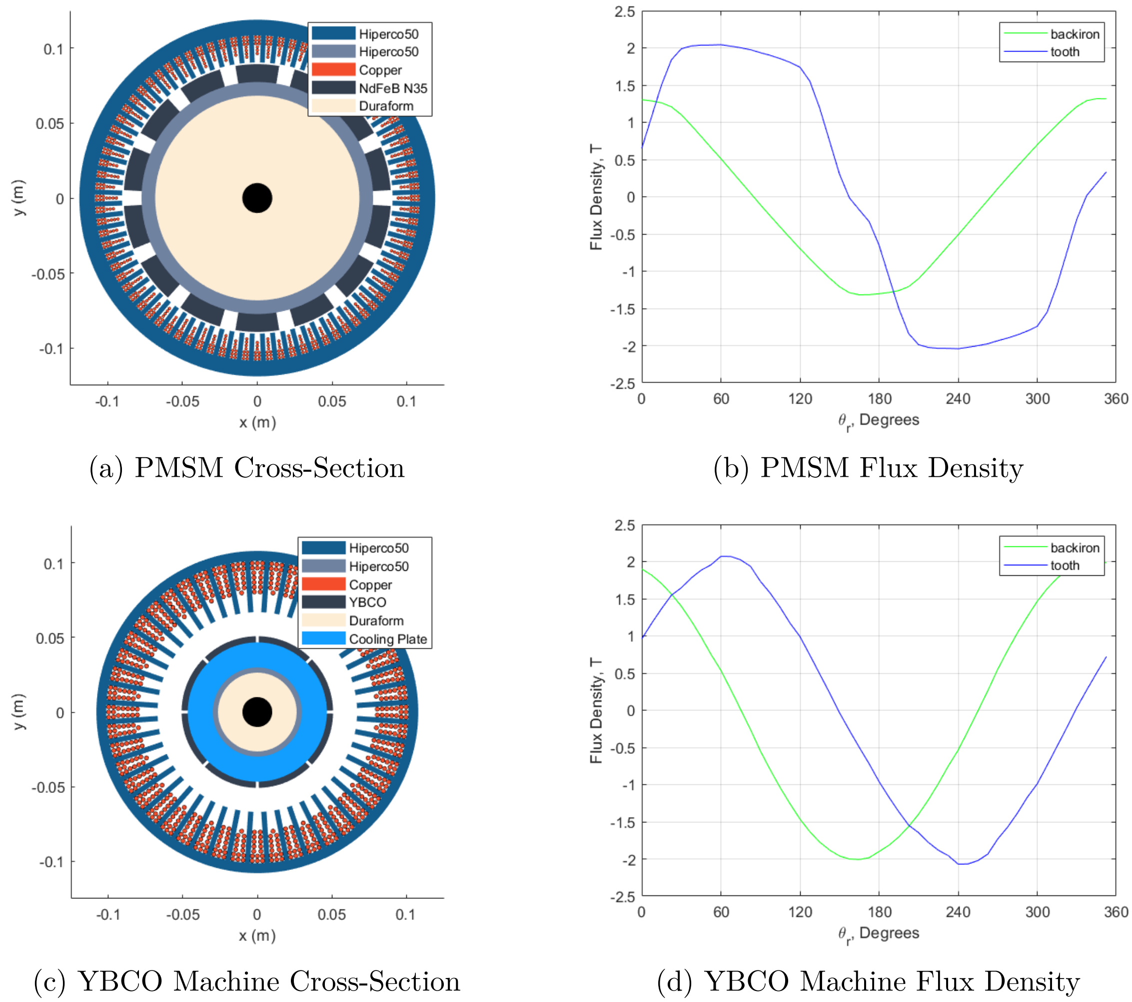

(a) PMSM Cross-Section

(b) PMSM Flux Density

(c) YBCO Machine Cross-Section

(d) YBCO Machine Flux Density

Figure 4.3. PMSM and YBCO Machine Comparison (10 kW)

due to the fact that the objectives of the YBCO machine optimization were to minimize the mass and loss of the entire system with cryocooler included, rather than the machines themselves. Therefore, the selected design for the YBCO machine likely is not an optimal design in terms of machine/inverter mass and loss alone. To provide a fair comparison of the two machines alone, another optimization of the YBCO machine could be performed without the cryocooler included.

From these initial optimizations for 10 kW machines, it is clear that the use of YBCO likely would not be warranted due to the size of the cryocooler system that would be required. Since the cryocooler accounted for the majority of the total mass and loss for the YBCO

Table 4.5. Machine Performance Comparison (10 kW)

Description	Symbol	PMSM	YBCO Machine
Power extracted by cooling plate	L	N/A	185 W
Machine Mass	m	16.184 kg	16.2 kg
Cryocooler Mass	m_{cryo}	N/A	39.3 kg
Total Mass	m_{tot}	16.184 kg	55.5 kg
Machine/Inverter Loss	P_l	351.9 W	496 W
Cryocooler Power	P_{cryo}	N/A	5.05 kW
Total Loss	$P_{l,tot}$	351.9 W	5.55 kW
Machine/Inverter Efficiency	η	96.65%	95.3%
Total Efficiency	η_{tot}	96.65%	64.3%

machines, additional optimizations for larger machines were performed to explore if there are power levels where the impact of the cryocooler is much less. Initially, optimizations were performed for both the PMSM and YBCO machine, with the output power requirement increased to 100 kW and 1 MW at a rotor speed of 1800 rpm.

The Pareto-optimal fronts for the optimizations performed for 100 kW machines are shown in Figure 4.4. Similar to the 10 kW case, the PMSM machines performed better than the YBCO machines. However, the impact of the cryocooler was indeed reduced. The PMSM designs along the front have an average mass of 172.1 kg with an average efficiency of 97.7%. In comparison, the YBCO machines and electric drives have an average mass of 149.5 kg and an efficiency of 97.6%. Taking the addition of the cryocooler into account, the average mass is 374.1 kg (m_{cryo} = 59.9% of total mass) and the average efficiency is 74.7%.

The Pareto-optimal fronts for the optimizations performed for the 1 MW machines are shown in Figure 4.5. For these designs, the dc source voltage was increased to 1 kV. No additional cooling of the windings was assumed, and the PMSM optimization initially had some difficulty in satisfying the constraint on the peak winding temperature. Thus, the maximum temperature in the stator windings was allowed to increase to 450 K in both optimizations. The PMSM machines again performed better than the YBCO machines, but

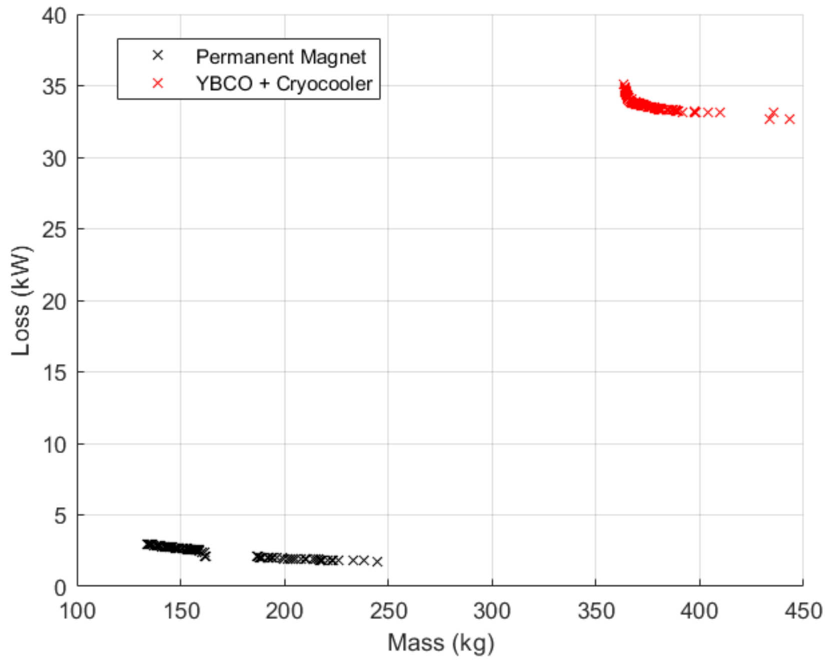

Figure 4.4. Pareto-Optimal Front (100 kW)

the impact of the cryocooler was further reduced. The PMSM designs along the front have an average mass of 1440.6 kg with an average efficiency of 99%. In comparison, the YBCO machines and electric drives have an average mass of 1167.2 kg and an efficiency of 98.8%. Taking the addition of the cryocooler into account, the average mass is 2295.6 kg (m_{cryo} = 49% of total mass) and the average efficiency is 85.4%.

A final optimization was performed for the two machines with the output power increased to 20 MW. In this optimization the mechanical rotor speed was reduced from 1800 rpm to 180 rpm, and with this slower rotational speed, the required torque is much higher. The dc source voltage was increased to 5 kV, and a peak winding temperature of 450 K was used, as in the 1 MW design studies. Additionally, in this design study a thin layer of insulation was added to the outer surface of the YBCO to reduce the amount of heat transferred from the surrounding air. The thickness of the insulation layer was added as an additional parameter for the YBCO machine. The two Pareto-optimal fronts are shown in Figure 4.6. From these two fronts it is seen that the YBCO machines and cryocooler system still have higher losses, but have considerably lower mass than the PMSM machines. The YBCO machines with

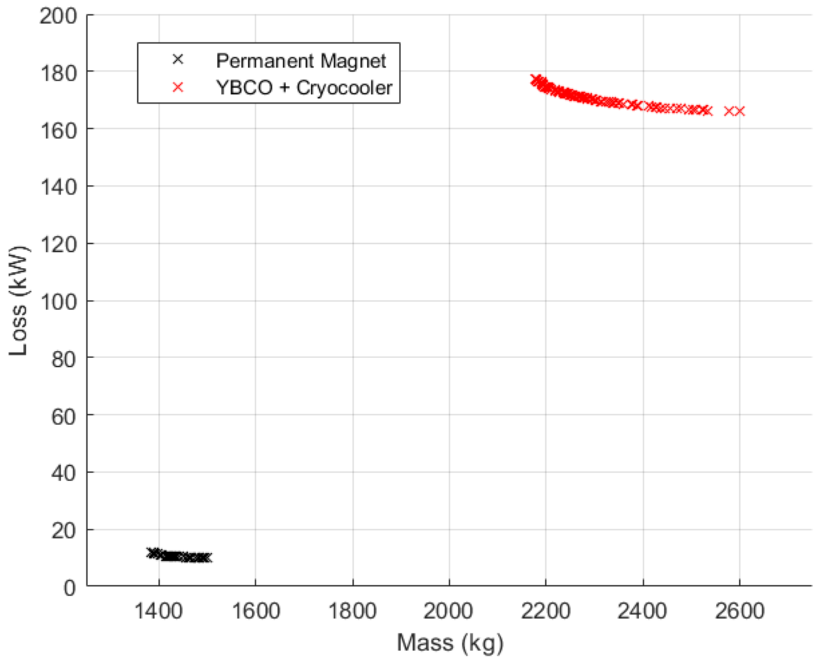

Figure 4.5. Pareto-Optimal Front (1 MW)

cryocooler included have an average mass of 59.3 metric tons with an average m_{cryo} of 10.2 metric tons (16.9% of total mass). The average overall efficiency is 93.1%, with an average machine/inverter efficiency of 99.8%. In comparison, the PMSM machines along the front have an average mass of 158.7 metric tons with an average efficiency of 99.7%.

An example design was selected from each Pareto-optimal front for comparison. The machine parameters are given in Table 4.6 and the performance of these two machines is compared in Table 4.7. It can be seen that the YBCO machine has very thin TFM pucks and an air gap of 1 mm (not including the insulation layer, which was assumed to be magnetically inert). Cross sections of these two machines and their flux density waveforms are shown in Figure 4.7.

The axial cross-sections in Figure 4.7 (c) and (d) show why the mass of the YBCO machine is much less than the PMSM. Even though the YBCO machine has a larger outer diameter, its active length is much smaller, resulting in a lower mass. The PMSMs along the Pareto-optimal front in Figure 4.6 have an average length of 197 cm and an average

Table 4.6. Machine Parameter Comparison (20 MW)

Description	**Symbol**	**PMSM**	**YBCO Machine**
Stator steel type	s_t	Hiperco50 (μ_r = 42,892)	Hiperco50 (μ_r = 42,892)
Rotor steel type	r_t	Hiperco50 (μ_r = 42,892)	Hiperco50 (μ_r = 42,892)
Conductor type	c_t	Copper	Copper
Magnet type	m_t	NdFeB N35 (B_r = 1.19 T)	TFM (B_{trap} = 2.627 T)
Poles	P	20	20
Slots	S_s	120	120
Shaft Radius	r_{rs}	25 cm	25 cm
Depth of inert region	d_{ri}	2.14 m	2.51 m
Depth of rotor backiron	d_{rb}	8.63 cm	5.89 cm
Depth of cooling plate	d_{cp}	N/A	6.01 cm
Depth of magnet	d_m	5.08 cm	0.2 cm
Thickness of insulation layer	t_{ins}	N/A	0.86 mm
Magnet fraction	α_m	71.8%	90%
Air gap	g	3.87 cm	1 mm
Depth of Tooth Base	d_{tb}	10.41 cm	17.63 cm
Tooth Fraction	α_t	25.7%	30.6%
Depth of stator backiron	d_{sb}	15.15 cm	6.41 cm
Active length	l	1.91 m	0.5 m
A-Phase Winding Pattern (1st Pole)	N_{as}	0 0 1 2 1 0	0 0 2 4 2 0
Conductor diameter	d_c	6.41 cm	6.09 cm
Q-Axis Current	I_{qs}^r	2.94 kA	2.39 kA
D-Axis Current	I_{ds}^r	-630 A	-224 A

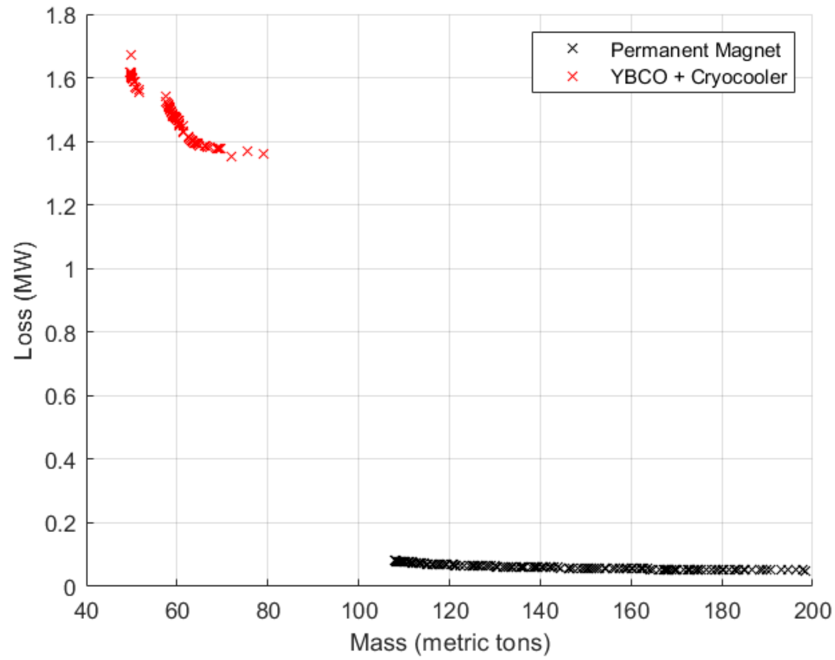

Figure 4.6. Pareto-Optimal Front (20 MW)

volume of 53.5 m^3 (only including active length of the machine). In comparison, the YBCO machines have an average active length of 50.4 cm and average volume of 16 m^3.

From these design studies it can be concluded that the use of YBCO within synchronous machines likely would not be warranted for machines at lower power levels. In the 10 kW and 100 kW optimizations, the mass of the cryocooler required to keep the YBCO below its critical temperature is larger than the machine itself. At the 1 MW power level the size of the YBCO machines and the cryocoolers are roughly the same. In each of these design studies, the power required by the cryocooler significantly increases the total input power required by the system, and therefore the use of YBCO likely would not be warranted as the standard PMSM has better performance. However, the impact of the cryocooler is seen to decrease as the output power of the YBCO machine increases. In the final optimization for 20 MW machines, the YBCO machine has a considerable advantage over the PMSM in terms of mass, with an overall efficiency greater than 90%. Due to this large reduction in mass, the use of YBCO in synchronous machines may be warranted for machines with high power levels such as the 20 MW machines shown herein.

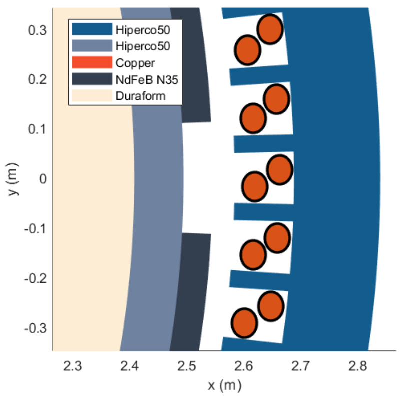

(a) PMSM Cross-Section

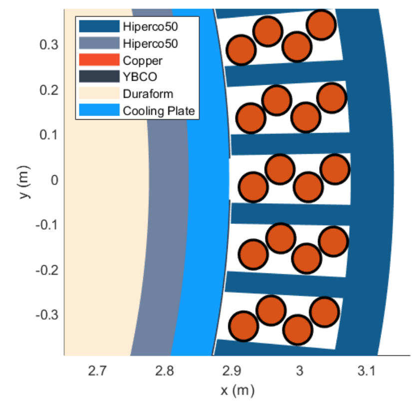

(b) YBCO Machine Cross-Section

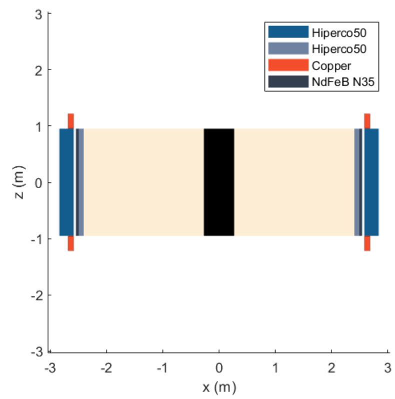

(c) PMSM Cross-Section

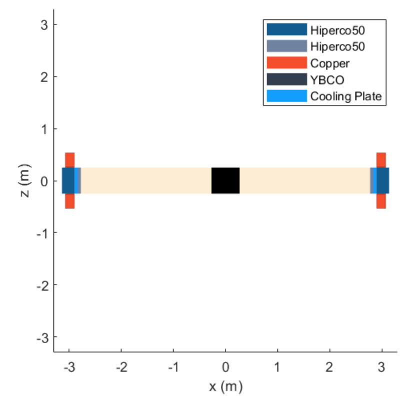

(d) YBCO Machine Cross-Section

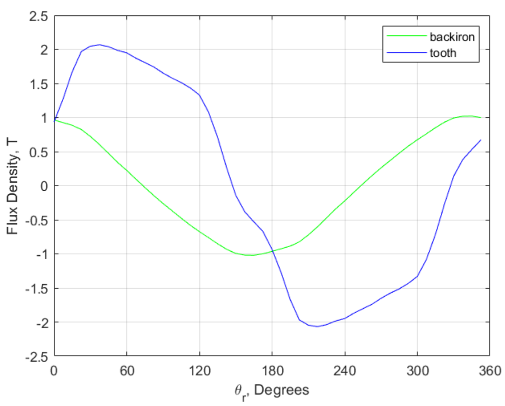

(e) PMSM Flux Density

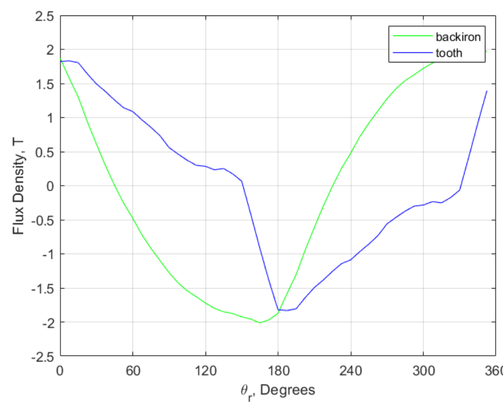

(f) YBCO Machine Flux Density

Figure 4.7. PMSM and YBCO Machine Comparison (20 MW)

Table 4.7. Machine Performance Comparison (20 MW)

Description	**Symbol**	**PMSM**	**YBCO Machine**
Power extracted by cooling plate	L	N/A	59.5 kW
Machine Mass	m	128.5 metric tons	49.2 metric tons
Cryocooler Mass	m_{cryo}	N/A	10.1 metric tons
Total Mass	m_{tot}	128.5 metric tons	59.4 metric tons
Machine/Inverter Loss	P_l	63.7 kW	38.6 kW
Cryocooler Power	P_{cryo}	N/A	1.44 MW
Total Loss	$P_{l,tot}$	63.7 kW	1.48 MW
Machine/Inverter Efficiency	η	99.7%	99.8%
Total Efficiency	η_{tot}	99.7%	93.2%

5. CONCLUSIONS

In this research, a Type-2 superconducting material (YBCO) was considered for use as a source of magnetic flux within synchronous machines. To evaluate its potential advantages over traditional permanent-magnet-based flux sources, an analytical model is first used to calculate the distribution of currents induced in the YBCO when it operates in a mixed-state. The currents are then used within a 2D MoM formulation [33] to evaluate the electromagnetic performance of YBCO-based machines. The MoM model is coupled to a thermal model that is used to determine the amount of power that must be extracted in order to keep the YBCO below a desired temperature. This power is then used to estimate the size of the cryocooler that would be required.

The MoM and thermal models were leveraged within a multi-objective design optimization to evaluate the tradeoffs between mass and loss in machines operating at power levels ranging from 10 kW - 20 MW. It was found that for lower-power applications, the size and power of the cryocooler led the overall mass/loss of the YBCO machines to greatly exceed that of a traditional PMSM. It was also found that as the required output power of the YBCO machines increases, the impact of the cryocooler on the system mass/loss is reduced. For example, in the 20 MW application, the YBCO machines had a much lower mass compared to traditional PMSMs.

Future work could focus on improving the thermal performance of the YBCO machine through minimizing the amount of power that must be extracted from the cryogenic cooling plate. One potential way of doing this would be to add insulation layers around the exterior of the YBCO to reduce the flow of heat across the air gap from the stator to the YBCO. A considerable fraction of the heat extracted by the cooling plate also comes from surfaces that are not in contact with the YBCO, specifically the rotor backiron and endcap air. Thus, additional research could be done to identify methods of insulating the cooling plate from the rest of the machine. Future research could also consider methods of magnetizing the YBCO material in-situ either using stator windings or additional magnetizing coils.

REFERENCES

[1] A. Sundaram, Y. Zhang, A. R. Knoll, D. Abraimov, P. Brownsey, M. Kasahara, G. M. Carota, R. Nakasaki, J. B. Cameron, G. Schwab, L. V. Hope, R. M. Schmidt, H. Kuraseko, T. Fukushima, and D. W. Hazelton, "2g HTS wires made on 30μm thick hastelloy substrate," *Superconductor Science and Technology*, vol. 29, no. 10, p. 104 007, Sep. 2016. DOI: 10.1088/0953-2048/29/10/104007. [Online]. Available: https://doi.org/10.1088/0953-2048/29/10/104007.

[2] M. Yagi, J. Liu, S. Mukoyama, T. Mitsuhashi, J. Teng, N. Hayakawa, X. Wang, A. Ishiyama, N. Amemiya, T. Hasegawa, T. Saitoh, O. Maruyama, and T. Ohkuma, "Experimental results of 275-kv 3-ka rebco hts power cable," *IEEE Transactions on Applied Superconductivity*, vol. 25, no. 3, pp. 1–5, 2015. DOI: 10.1109/TASC.2014.2385960.

[3] M. Iwakuma, A. Tomioka, M. Konno, Y. Hase, T. Satou, Y. Iijima, T. Saitoh, Y. Yamada, T. Izumi, and Y. Shiohara, "Development of a 15 kw motor with a fixed ybco superconducting field winding," *IEEE Transactions on Applied Superconductivity*, vol. 17, no. 2, pp. 1607–1610, 2007. DOI: 10.1109/TASC.2007.898480.

[4] M. Iwakuma, Y. Hase, T. Satou, A. Tomioka, M. Konno, Y. Iijima, T. Saitoh, Y. Yamada, T. Izumi, and Y. Shiohara, "Development of a 7.5 kw ybco superconducting synchronous motor," *IEEE Transactions on Applied Superconductivity*, vol. 18, no. 2, pp. 689–692, 2008. DOI: 10.1109/TASC.2008.920564.

[5] P. J. Masson, M. Breschi, P. Tixador, and C. A. Luongo, "Design of hts axial flux motor for aircraft propulsion," *IEEE Transactions on Applied Superconductivity*, vol. 17, no. 2, pp. 1533–1536, 2007. DOI: 10.1109/TASC.2007.898120.

[6] J. Lopez, J. Lloberas, R. Maynou, X. Granados, R. Bosch, X. Obradors, and R. Torres, "Ac three-phase axial flux motor with magnetized superconductors," *IEEE Transactions on Applied Superconductivity*, vol. 17, no. 2, pp. 1633–1636, 2007. DOI: 10.1109/TASC.2007.898361.

[7] B. Oswald, M. Krone, M. Soll, T. Strasser, J. Oswald, K. .-. Best, W. Gawalek, and L. Kovalev, "Superconducting reluctance motors with ybco bulk material," *IEEE Transactions on Applied Superconductivity*, vol. 9, no. 2, pp. 1201–1204, 1999. DOI: 10.1109/77.783515.

[8] J. X. Jin, L. H. Zheng, Y. G. Guo, and J. G. Zhu, "Performance characteristics of an hts linear synchronous motor with hts bulk magnet secondary," *IEEE Transactions on Industry Applications*, vol. 47, no. 6, pp. 2469–2477, 2011. DOI: 10.1109/TIA.2011.2168934.

[9] W. Xian, Y. Yan, W. Yuan, R. Pei, and T. A. Coombs, "Pulsed field magnetization of a high temperature superconducting motor," *IEEE Transactions on Applied Superconductivity*, vol. 21, no. 3, pp. 1171–1174, 2011. DOI: 10.1109/TASC.2010.2092745.

[10] X. Feng, G. Gao, K. Davey, M. Werst, R. Hebner, R. Weinstein, D. Parks, and R. Sawh, "Radial flux high temperature superconductor motor using bulk trapped field magnets," in *2009 IEEE International Electric Machines and Drives Conference*, 2009, pp. 458–464. DOI: 10.1109/IEMDC.2009.5075246.

[11] K. Davey, R. Weinstein, R. Sawh, and D. Parks, "The use of very thin tfms in electromechanical devices," *IEEE Transactions on Applied Superconductivity*, vol. 29, no. 5, pp. 1–5, 2019. DOI: 10.1109/TASC.2019.2902187.

[12] G. G. Sotelo, R. A. H. de Oliveira, F. S. Costa, D. H. N. Dias, R. de Andrade, and R. M. Stephan, "A full scale superconducting magnetic levitation (maglev) vehicle operational line," *IEEE Transactions on Applied Superconductivity*, vol. 25, no. 3, pp. 1–5, 2015. DOI: 10.1109/TASC.2014.2371432.

[13] P. J. da Costa Branco and J. A. Dente, "Design and experiment of a new maglev design using zero-field-cooled ybco superconductors," *IEEE Transactions on Industrial Electronics*, vol. 59, no. 11, pp. 4120–4127, 2012. DOI: 10.1109/TIE.2011.2174541.

[14] *Helium*. [Online]. Available: https://www.britannica.com/science/helium-chemical-element.

[15] J. G. Bednorz and K. A. Müller, "Possible hightc superconductivity in the ba—la—cu—o system," *Zeitschrift für Physik B Condensed Matter*, vol. 64, no. 2, pp. 189–193, Jun. 1986, ISSN: 1431-584X. DOI: 10.1007/BF01303701. [Online]. Available: https://doi.org/10.1007/BF01303701.

[16] M. K. Wu, J. R. Ashburn, C. J. Torng, P. H. Hor, R. L. Meng, L. Gao, Z. J. Huang, Y. Q. Wang, and C. W. Chu, "Superconductivity at 93 k in a new mixed-phase y-ba-cu-o compound system at ambient pressure," *Phys. Rev. Lett.*, vol. 58, pp. 908–910, 2 Mar. 1987. DOI: 10.1103/PhysRevLett.58.908. [Online]. Available: https://link.aps.org/doi/10.1103/PhysRevLett.58.908.

[17] P. J. Lee, "Superconductivity and magnetism," in *Engineering Superconductivity*. 2001, pp. 1–185. DOI: 10.1109/9780470547175.ch1.

[18] B. D. Cullity and C. D. Graham, "Magnetic properties of superconductors," in *Introduction to Magnetic Materials*. 2009, pp. 517–526. DOI: 10.1002/9780470386323.ch16.

[19] A. A. Abrikosov, "On the magnetic properties of superconductors of the second group," *JTEP*, vol. 5, pp. 1174–1182, 15 Dec. 1957.

[20] J. Bardeen and M. J. Stephen, “Theory of the motion of vortices in superconductors,” eng, *Physical review*, vol. 140, no. 4A, A1197–A1207, 1965, ISSN: 0031-899X.

[21] M. N. Wilson, *Superconducting magnets*, eng, ser. Monographs on cryogenics ; [2]. Oxford [Oxfordshire] : New York: Clarendon Press ; Oxford University Press, 1983, ISBN: 0198548052.

[22] M. Tomita and M. Murakami, “High-temperature superconductor bulk magnets that can trap magnetic fields of over 17 tesla at 29 k,” *Nature*, vol. 421, no. 6922, pp. 517–520, Jan. 2003. DOI: 10.1038/nature01350.

[23] A. Patel, A. Baskys, T. Mitchell-Williams, A. McCaul, W. Coniglio, J. Hänisch, M. Lao, and B. A. Glowacki, “A trapped field of 17.7 t in a stack of high temperature superconducting tape,” eng, *Superconductor science & technology*, vol. 31, no. 9, p. 9, 2018, ISSN: 0953-2048.

[24] N. Hari Babu, K. Iida, and D. Cardwell, “Enhanced magnetic flux pinning in nano-composite y–ba–cu–o superconductors,” *Physica C: Superconductivity and its Applications*, vol. 445-448, pp. 353–356, 2006, Proceedings of the 18th International Symposium on Superconductivity (ISS 2005), ISSN: 0921-4534. DOI: https://doi.org/10.1016/j.physc.2006.04.081. [Online]. Available: http://www.sciencedirect.com/science/article/pii/S0921453406003170.

[25] J. W. Kell and P. N. Barnes, “Flux pinning enhancement of ybco films by y and ba site doping at minute concentrations,” *MRS Proceedings*, vol. 1001, pp. 1001–M13–03, 2007. DOI: 10.1557/PROC-1001-M13-03.

[26] Y. B. Kim, C. F. Hempstead, and A. R. Strnad, “Critical persistent currents in hard superconductors,” *Phys. Rev. Lett.*, vol. 9, pp. 306–309, 7 Oct. 1962. DOI: 10.1103/PhysRevLett.9.306. [Online]. Available: https://link.aps.org/doi/10.1103/PhysRevLett.9.306.

[27] M. R. Beasley, R. Labusch, and W. W. Webb, “Flux creep in type-ii superconductors,” eng, *Physical review*, vol. 181, no. 2, pp. 682–700, 1969, ISSN: 0031-899X.

[28] M. E. Ladd, P. Bachert, M. Meyerspeer, E. Moser, A. M. Nagel, D. G. Norris, S. Schmitter, O. Speck, S. Straub, and M. Zaiss, “Pros and cons of ultra-high-field mri/mrs for human application,” *Progress in Nuclear Magnetic Resonance Spectroscopy*, vol. 109, pp. 1–50, 2018, ISSN: 0079-6565. DOI: https://doi.org/10.1016/j.pnmrs.2018.06.001. [Online]. Available: https://www.sciencedirect.com/science/article/pii/S007965651830013X.

[29] S. T. Anderson, "Economics, helium, and the u.s. federal helium reserve: Summary and outlook," *Natural Resources Research*, vol. 27, no. 4, pp. 455–477, Oct. 2018, ISSN: 1573-8981. DOI: 10.1007/s11053-017-9359-y. [Online]. Available: https://doi.org/10.1007/s11053-017-9359-y.

[30] B. J. Parkinson, R. Slade, M. J. D. Mallett, and V. Chamritski, "Development of a cryogen free 1.5 t ybco hts magnet for mri," *IEEE Transactions on Applied Superconductivity*, vol. 23, no. 3, pp. 4 400 405–4 400 405, 2013. DOI: 10.1109/TASC.2012.2235893.

[31] A. Patel, A. Baskys, S. C. Hopkins, V. Kalitka, A. Molodyk, and B. A. Glowacki, "Pulsed-field magnetization of superconducting tape stacks for motor applications," *IEEE Transactions on Applied Superconductivity*, vol. 25, no. 3, pp. 1–5, 2015. DOI: 10.1109/TASC.2015.2389142.

[32] S. D. Sudhoff, *Power Magnetic Devices: A Multi-Objective Design Approach*, eng, 1st ed., ser. IEEE Press Series on Power Engineering. New York: Wiley, 2014, ISBN: 9781118489994.

[33] D. C. Horvath, S. D. Pekarek, and R. A. Howard, "Analysis and design of electric machines using 2d method of moments," in *2019 IEEE International Electric Machines Drives Conference (IEMDC)*, 2019, pp. 476–483. DOI: 10.1109/IEMDC.2019.8785130.

[34] R. Howard, A. Brovont, and S. Pekarek, "Analytical evaluation of 2-d flux integral for magnetostatic galerkin method of moments," *IEEE Transactions on Magnetics*, vol. 52, no. 4, pp. 1–8, 2016. DOI: 10.1109/TMAG.2015.2501280.

[35] R. Howard and S. Pekarek, "Two-dimensional galerkin magnetostatic method of moments," *IEEE Transactions on Magnetics*, vol. 53, no. 12, pp. 1–6, 2017. DOI: 10.1109/TMAG.2017.2741449.

[36] R. A. Howard, "Derivation, application, and evaluation of the method of moments to solve two-dimensional magnetostatic problems," Ph.D. dissertation, Purdue University, West Lafayette, IN, 2013.

[37] D. C. Horvath, "Analysis and design of electric machines using 2d method of moments," Ph.D. dissertation, Purdue University, West Lafayette, IN, 2019.

[38] D. Horvath, R. Howard, and S. Pekarek, "Lorentz force/torque calculation in 2-d method of moments," *IEEE Transactions on Magnetics*, vol. 56, no. 8, pp. 1–8, 2020. DOI: 10.1109/TMAG.2020.3002982.

[39] C. P. Bean, "Magnetization of hard superconductors," eng, *Physical review letters*, vol. 8, no. 6, pp. 250–253, 1962, ISSN: 0031-9007.

[40] C. P. BEAN, “Magnetization of high-field superconductors,” eng, *Reviews of modern physics*, vol. 36, no. 1, pp. 31–39, 1964, ISSN: 0034-6861.

[41] H. Theuss, A. Forkl, and H. Kronmüller, “Current density and magnetic field distribution in hard thin film superconductors,” *Physica C: Superconductivity*, vol. 190, no. 3, pp. 345–352, 1992, ISSN: 0921-4534. DOI: https://doi.org/10.1016/0921-4534(92)90617-L. [Online]. Available: https://www.sciencedirect.com/science/article/pii/092145349290617L.

[42] A. Forkl, “Magnetic flux distribution in single crystalline, ceramic and thin film high-tc-superconductors,” eng, *Physica scripta*, vol. 1993, pp. 148–158, 1993, ISSN: 1402-4896.

[43] E. H. Brandt, M. V. Indenbom, and A. Forkl, “Type-ii superconducting strip in perpendicular magnetic field,” eng, *Europhysics letters*, vol. 22, no. 9, pp. 735–740, 1993, ISSN: 0295-5075.

[44] E. Brandt, “Superconductors of finite thickness in a perpendicular magnetic field: Strips and slabs,” eng, *Physical review. B, Condensed matter*, vol. 54, no. 6, pp. 4246–4264, 1996, ISSN: 0163-1829.

[45] L. Prigozhin, “Analysis of critical-state problems in type-ii superconductivity,” *IEEE Transactions on Applied Superconductivity*, vol. 7, no. 4, pp. 3866–3873, 1997. DOI: 10.1109/77.659440.

[46] G. Barnes, M. McCulloch, and D. Dew-Hughes, “Computer modelling of type II superconductors in applications,” *Superconductor Science and Technology*, vol. 12, no. 8, pp. 518–522, Jul. 1999. DOI: 10.1088/0953-2048/12/8/308. [Online]. Available: https://doi.org/10.1088/0953-2048/12/8/308.

[47] C. T.A., C. A.M., M. A., and E. M., “A fast algorithm for calculating the critical state in superconductors,” *COMPEL - The international journal for computation and mathematics in electrical and electronic engineering*, vol. 20, no. 1, pp. 240–252, Jan. 2001.

[48] K. R. Davey, R. Weinstein, D. Parks, and R. Sawh, “Simulating the trapped b field in bulk superconductors using a mutual inductance coupling technique,” *IEEE Transactions on Magnetics*, vol. 49, no. 3, pp. 1153–1158, 2013. DOI: 10.1109/TMAG.2012.2220558.

[49] K. Davey, R. Weinstein, D. Parks, and R. Sawh, “Predicting the trapped b field in bulk superconductors using critical state models,” *IEEE Transactions on Magnetics*, vol. 50, no. 1, pp. 1–7, 2014. DOI: 10.1109/TMAG.2013.2282368.

[50] R. Weinstein, D. Parks, R. Sawh, K. Davey, and K. Carpenter, "Observation of a bean model limit—a large decrease in required applied activation field for tfms," *IEEE Transactions on Applied Superconductivity*, vol. 25, no. 3, pp. 1–6, 2015. DOI: 10.1109/TASC.2014.2366722.

[51] R.-P. Sawh, R. Weinstein, K. Carpenter, D. Parks, and K. Davey, "Production run of 2 cm diameter YBCO trapped field magnets with surface field of 2 t at 77 k," *Superconductor Science and Technology*, vol. 26, no. 10, p. 105 014, Aug. 2013. DOI: 10.1088/0953-2048/26/10/105014. [Online]. Available: https://doi.org/10.1088/0953-2048/26/10/105014.

[52] S. D. Sudhoff, *Thermal equivalent circuit toolbox 2.0*. [Online]. Available: https://engineering.purdue.edu/ECE/Research/Areas/PES/Software/thermal_equivalent_toolbox.

[53] H. Fujishiro, M. Ikebe, T. Naito, K. Noto, S. Kohayashi, and S. Yoshizawa, "Anisotropic thermal diffusivity and conductivity of YBCO(123) and YBCO(211) mixed crystals. i," *Japanese Journal of Applied Physics*, vol. 33, no. Part 1, No. 9A, pp. 4965–4970, Sep. 1994. DOI: 10.1143/jjap.33.4965. [Online]. Available: https://doi.org/10.1143/jjap.33.4965.

[54] *Duraform pa (sls)*, Jan. 2021. [Online]. Available: https://www.3dsystems.com/materials/duraform-pa.

[55] P. H. MELLOR, D. ROBERTS, and D. R. TURNER, "Lumped parameter thermal model for electrical machines of tefc design," eng, *IEE proceedings. Part B, Electric power applications*, vol. 138, no. 5, pp. 205–218, 1991, ISSN: 0143-7038.

[56] J. Gibbins, *Thermal contact resistance of polymer interfaces*, eng, 2006.

[57] S. Touhami, Y. Bertin, Y. Lefèvre, J.-F. Llibre, C. Henaux, and M. Fenot, "Lumped parameter thermal model of permanent magnet synchronous machines," in *Electrimacs 2017*, Toulouse, FR, 2017, pp. 1–6. [Online]. Available: https://oatao.univ-toulouse.fr/18499/.

[58] S. D. Sudhoff, *Genetic optimization system engineering toolbox 2.6*. [Online]. Available: https://engineering.purdue.edu/ECE/Research/Areas/PES/Software/genetic-optimization-toolbox-2.6.

[59] J. L. Smith, J. S. Brooks, C. M. Fowler, B. L. Freeman, J. D. Goettee, W. L. Hults, J. C. King, P. M. Mankiewich, E. I. De Obaldia, M. L. O'Malley, D. G. Rickel, and W. J. Skocpol, "Low-temperature critical field of ybco," *Journal of Superconductivity*,

[60] T. Sekitani, N. Miura, S. Ikeda, Y. Matsuda, and Y. Shiohara, "Upper critical field for optimally-doped yba2cu3o7− ," *Physica B: Condensed Matter*, vol. 346-347, pp. 319–324, 2004, Proceedings of the 7th International Symposium on Research in High Magnetic Fields, ISSN: 0921-4526. DOI: https://doi.org/10.1016/j.physb.2004.01.098. [Online]. Available: https://www.sciencedirect.com/science/article/pii/S0921452604000894.

[61] I.-G. Chen, J. Liu, Y. Ren, R. Weinstein, G. Kozlowski, and C. Oberly, "Quasipermanent magnets of high temperature superconductor - temperature dependence," *Applied Physics Letters*, vol. 62, Jul. 1993. DOI: 10.1063/1.109073.

[62] O. Vakaliuk, F. Werfel, J. Jaroszynski, and B. Halbedel, "Trapped field potential of commercial y-ba-cu-o bulk superconductors designed for applications," *Superconductor Science and Technology*, vol. 33, p. 095 005, Sep. 2020. DOI: 10.1088/1361-6668/ab9fc4.